ASCE

Multidirectional Vibroseis Shaking and Controlled Blasting to Determine the Dynamic In Situ Response of a Low-Plasticity Silt Deposit

Amalesh Jana[1]; Ali Dadashiserej[2]; Benchen Zhang[3]; Armin W. Stuedlein, M.ASCE[4]; T. Matthew Evans, M.ASCE[5]; Kenneth H. Stokoe II, Dist.M.ASCE[6]; and Brady R. Cox, M.ASCE[7]

Abstract: In this paper, efforts to characterize and compare the full-scale in situ three-dimensional (3D) dynamic response of a low-plasticity silt deposit to multidirectional loading from two different sources, a vibroseis shaker named T-Rex and controlled blasting, are presented. Horizontal vibroseis shaking at a frequency, f, of 10 Hz, produced dynamic responses in the silt that ranged from linear-elastic to nonlinear-inelastic, inducing maximum equivalent direct simple shear (DSS) shear strains, $\gamma_{DSS,max}$, up to 0.15% and residual excess pore pressure ratios, $r_{u,r}$, of 14.1%. Blast-induced shear waves with predominant frequencies ranging from 9.6 to 14.6 Hz excited nonlinear-elastic and nonlinear-inelastic responses in the silt deposit, with $\gamma_{DSS,max}$ of 1.14% and maximum $r_{u,r}$ of 61%. Importantly, these responses were observed to be minimally influenced by high frequency compression waves. Multidirectional loading, and excess pore pressure, u_e, migration and impedance were identified as the predominant factors for achieving the large $r_{u,r}$ in the silt deposit from these two in situ testing techniques. The cyclic threshold shear strain, γ_{tp}, to trigger $r_{u,r}$ observed from the T-Rex shaking equaled 0.007% to 0.011% and varied with the initial soil stiffness. The two testing techniques demonstrated that the in-situ shear modulus, G, reduced to 90% of the maximum shear modulus, G_{max}, at $\gamma_{DSS,max} \approx \gamma_{tp}$, whereas by $\gamma_{DSS,max} \approx 1\%$, G further reduced to 10 to 30% of G_{max} corresponding to $r_{u,r}$ of ~60%. Changes in soil fabric were quantified using small-strain shear-wave velocity measurements performed before and/or upon initiation and after each stage of dynamic testing, and were linked to the observed increase and decrease in γ_{tp} for the shallower and deeper 3D elements, respectively, following T-Rex shaking. The side-by-side comparison of the dynamic responses and soil properties derived from these two distinctly different field-testing techniques validate the use of controlled blasting for quantifying in situ dynamic soil properties and responses. **DOI: 10.1061/(ASCE)GT.1943-5606.0002924.**

Introduction

The terms liquefaction, cyclic mobility, and cyclic softening have been used to describe the failure mechanisms of soils that may arise from seismic loading of saturated soils (Seed and Idriss 1971; Dobry et al. 1982; Andrus and Stokoe 2000; Bray and Sancio 2006; Idriss and Boulanger 2008). Quantified in situ observations of these coupled fluid-mechanical phenomena linking the loading (i.e., stresses and strains) from earthquake ground motions to destabilizing excess pore pressures, u_e, are limited, although inferential studies have proven informative (e.g., Zeghal and Elgamal 1994). Laboratory element tests have therefore been extensively used to simulate analogous cyclic loading of soils for the purposes of seismic performance assessment (Lee and Seed 1967; Koester 1994; Vaid 1994; Polito and Martin 2001); yet the difficulty in obtaining truly undisturbed samples of many soil types of interest has led to reliance on reconstituted soils, the method of preparation of which strongly affects their responses (Park and Silver 1975; Ladd 1977; Mulilis et al. 1977). The difficulty replicating the natural in situ soil fabric, stress state, and drainage conditions in the laboratory has been noted by the profession for many decades (Mulilis et al. 1977; Dobry and Abdoun 2015; Adamidis and Madabhushi 2018; Jana and Stuedlein 2021a, b). In situ u_e generation is more rapid than typically observed in conventional undrained or constant volume laboratory tests due to the two-dimensional (2D) or three-dimensional (3D) nature of earthquake ground motions (Seed et al. 1978) and redistribution of pore pressures during shaking (Cubrinovski et al. 2019), which are also difficult to simulate in the laboratory (Dobry and Abdoun 2015). The few laboratory studies on multidirectional loading confirmed greater u_e generation and lower cyclic resistance in sand and silt relative to unidirectional loading (Seed et al. 1978; Boulanger 1990; Kammerer et al. 2002; Matsuda et al. 2013). Few direct in situ multidirectional measurements of shear strain and the resulting u_e exist.

Laboratory cyclic testing of natural intact specimens continues to represent the best practice for establishing the dynamic response of transitional nonplastic and low-plasticity silts to identify the roles of depositional environment, plasticity (i.e., mineralogy), fines content, and stress history on cyclic resistance, as demonstrated by

[1]Postdoctoral Researcher, School of Civil and Construction Engineering, Oregon State Univ., 101 Kearney Hall, Corvallis, OR 97330.
[2]Research Assistant, School of Civil and Construction Engineering, Oregon State Univ., 101 Kearney Hall, Corvallis, OR 97330.
[3]Senior Staff Engineer, Beyond Engineering and Testing, 3801 Doris Lane Suite B, Round Rock, TX 78664.
[4]Professor, School of Civil and Construction Engineering, Oregon State Univ., 101 Kearney Hall, Corvallis, OR 97330 (corresponding author). ORCID: https://orcid.org/0000-0002-6265-9906. Email: armin.stuedlein@oregonstate.edu
[5]Professor, School of Civil and Construction Engineering, Oregon State Univ., 101 Kearney Hall, Corvallis, OR 97330.
[6]Professor, Dept. of Civil, Architectural, and Environmental Engineering, Univ. of Texas, Austin, TX 78712.
[7]Professor, Dept. of Civil and Environmental Engineering, Utah State Univ., Logan, UT 84322.

Note. This manuscript was submitted on September 6, 2021; approved on July 25, 2022; published online on January 12, 2023. Discussion period open until June 12, 2023; separate discussions must be submitted for individual papers. This paper is part of the ***Journal of Geotechnical and Geoenvironmental Engineering***, © ASCE, ISSN 1090-0241.

Sanin and Wijewickreme (2006), Dahl et al. (2014), Wijewickreme et al. (2019), Jana and Stuedlein (2021c), and Stuedlein et al. (2023). However, some amount of disturbance is inevitable, especially for low-plasticity silt (Boone 2010; DeJong et al. 2018), such that capturing the true in situ response of such soils in the laboratory is difficult (Beyzaei et al. 2018, 2020). False-positive liquefaction predictions of silty soils using the cone penetration test (CPT)-based liquefaction triggering analysis were notable following the Canterbury earthquake sequence (e.g., Cubrinovski et al. 2012; Cox et al. 2017; Yost et al. 2019; Cappellaro et al. 2021), indicating the need to improve our understanding of the in situ seismic response of silty soils, including (1) the degradation of shear stiffness from the linear-elastic to nonlinear-inelastic regimes, (2) the triggering of destabilizing u_e, (3) the effects of partially saturated zones below the groundwater table, and (4) potential postshaking consequences such as reconsolidation settlements or sustained loss of strength.

In situ coupled cyclic shear-induced u_e and/or soil nonlinearity has been effectively observed using the large vibroseis shakers at Natural Hazards Engineering Research Infrastructure Center at the University of Texas, Austin (NHERI@UTexas) (Stokoe et al. 2017) applied to instrumented deposits of sands, silty sands, and unsaturated silts (Rathje et al. 2001; Kurtulus and Stokoe 2008; Cox et al. 2009; Roberts et al. 2016). Recently, controlled blasting implementing the instrumentation protocols used during previous T-Rex shaking studies has been deployed as a separate field-testing technique to obtain in situ dynamic properties, triggering relationships, and shear modulus nonlinearity and degradation of soil deposits (Jana et al. 2021), including a medium-stiff plastic silt deposit at a depth of 10 m (Jana and Stuedlein 2021a) and at a depth of 25 m in a medium-dense sand deposit (Jana and Stuedlein 2021b). However, a direct comparison of the dynamic responses and soil properties derived from these two distinctly different field techniques on the same instrumented array has yet to be evaluated, the results of which could lend increased confidence in both approaches.

This paper describes the in situ, coupled, dynamic shear-induced excess pore pressure and nonlinear inelasticity of an instrumented low-plasticity silt deposit at the Port of Longview, Washington, evaluated using a large mobile vibroseis shaker named T-Rex and the controlled blasting testing technique. The main goals of this work were to (1) observe and quantify the in situ dynamic response of low-plasticity silts, (2) compare the dynamic soil properties and responses derived from these two highly distinctly different field-testing techniques, and (3) identify similarities and differences between the field- and laboratory-derived behaviors. In this paper, the two first two goals are addressed, namely demonstrating the similarities and differences between the two field-testing techniques, providing an improved understanding of the application of field-testing techniques to geotechnical earthquake engineering problems, and quantification of the effect of prestraining on soil fabric and the strain necessary to trigger excess pore pressures.

Experimental Setting and Soil Characterization

Several distinct instrumented test panels were installed in the shallow sands and silts at Barlow Point at the Port of Longview, Longview, Washington (e.g., Zhang et al. 2021; Dadashiserej et al. 2022b). In this paper, the response at one such panel, termed the Oregon State University (OSU) Blast Array is described. The experimental layout of the array, subsurface explorations, and in situ tests are shown in Fig. 1, which illustrates the types and locations of the instruments, blast casings, CPTs and mud-rotary boreholes advanced to obtain thin-walled tube samples. Cone penetration tests CPT-1 through CPT-3 were conducted on the day of in situ dynamic testing with T-Rex and are used, along with soil cuttings and thin-walled tube samples, to identify the stratigraphy along Section A-A′ (Fig. 1) shown in Fig. 2.

The subsurface at the instrumented array consists of dense silty sand with gravel fill to a depth of 0.4 m, followed by moist medium-stiff sandy silt (ML) grading to soft clayey silt to silty clay (ML to CL) that extends to a depth of approximately 1 m. A 1.2-m-thick deposit of moist grading to wet very soft to soft clayey silt to silty clay (MH to CH) followed. This 1.2-m-thick deposit is underlain by an approximately 0.6-m-thick layer of wet, soft to medium-stiff clayey silt (ML) interbedded with occasional stringers of sandy silt. A thick deposit of wet, very soft clayey silt was observed extending to the depth of the explorations; nearby explorations suggest that this deposit extends to the underlying basalt bedrock encountered at depths of 60 to 80 m below the ground surface. The groundwater table was observed 1.45 m below the ground surface during CPT Soundings 1 to 3.

The plasticity index (PI) and CPT-based (i.e., correlated) overconsolidation ratio (OCR) (using Mayne 2007) varied from 9 to 19 and 2.8 to 5.8 respectively, over the instrumented depths of the silt

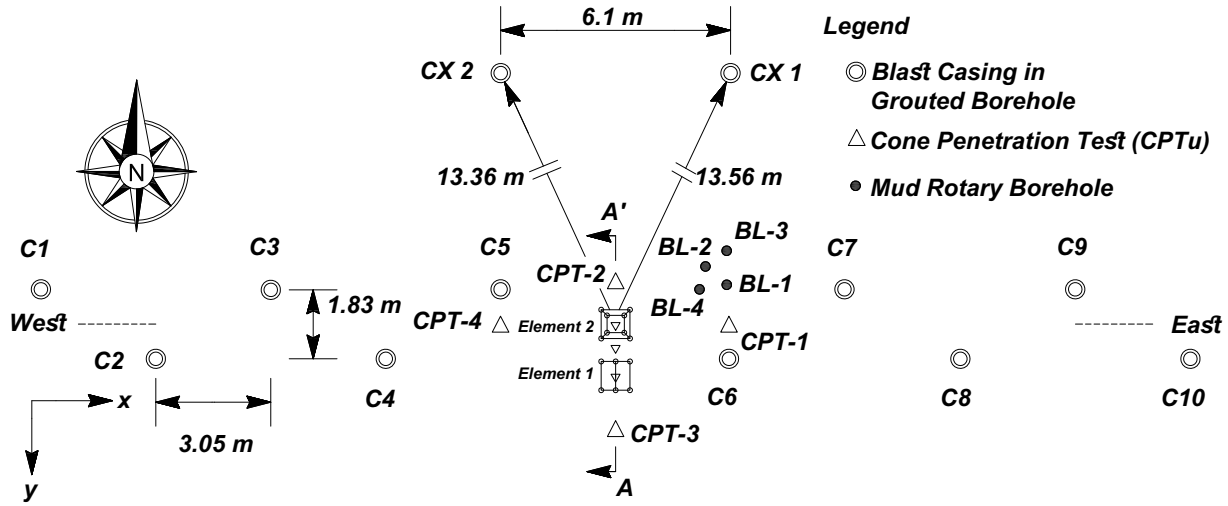

Fig. 1. Site and exploration plan for the OSU Blast Array (all distances in meters). The x- and y-coordinate system indicates the positive horizontal directions of the triaxial geophones.

J. Geotech. Geoenviron. Eng., 2023, 149(3): 04023006

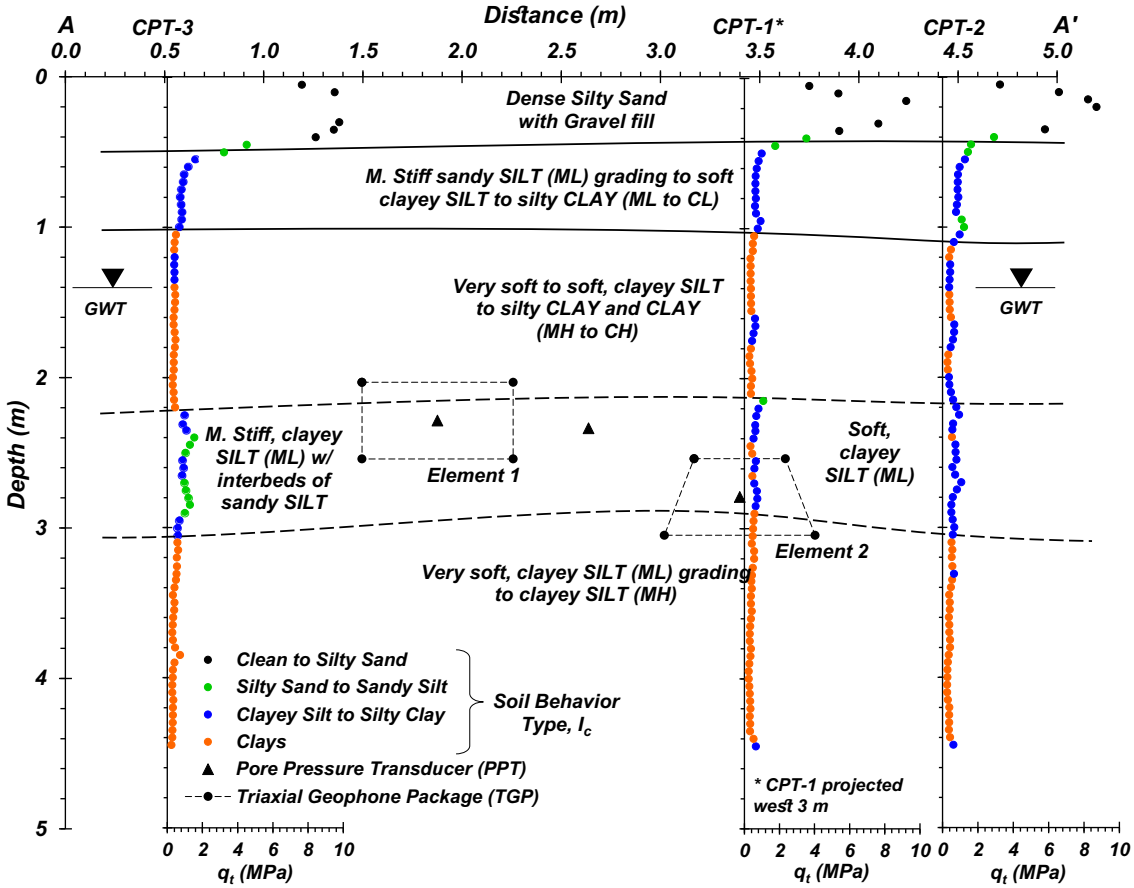

Fig. 2. Subsurface stratigraphy at Section A-A′ (Fig. 1) facing west at the OSU Blast Array indicating the locations of the array elements, groundwater table, and CPT results.

deposit (i.e., 2.03 to 3.05 m), whereas the laboratory-based OCR appeared relatively constant, ranging from 4.0 to 4.5 (Fig. S1). The variations of the corrected cone tip resistance q_t, soil behavior type index I_c (Robertson 2009), PI, fines content (FC), laboratory- and CPT-based OCR, and downhole and CPT-based (correlated using Andrus et al. 2007) small-strain shear-wave velocity V_s with depth are shown in Fig. S1. The average in situ P-wave velocity V_p of the soil over the instrumented depths is 1,069 m/s, indicating that the soil was nearly fully saturated (Stokoe and Santamarina 2000; Jana and Stuedlein 2021c). The subsurface profile indicates variability in the aforementioned soil properties, which appears to have influenced the dynamic in situ test responses of the low-plastic silt (ML) deposit as described subsequently.

Experimental Program

Instrumentation

Fourteen triaxial geophone packages (TGPs) were installed using direct-push techniques to form several novel three-dimensional instrumentation arrays (i.e., elements, as indicated in Figs. 1–3). Each TGP consisted of three geophones (Geospace model GS-14-L3-28, Geospace Technologies, Houston) arranged to measure particle velocity in the three orthogonal directions of interest, and one dual axis microelectromechanical systems (MEMS) accelerometer (ADXL model 103, Analog Devices, Wilmington, Massachusetts) to measure the as-built static tilt of each package in two orthogonal directions. The unit weight of each monolithic TGP was 14.3 kN/m^3, similar to the soil unit weight, providing a similar response to buoyancy as the surrounding soils. Separate pore pressure transducers (PPTs) (Model STS ATM.1ST/N, Sensor Technik Sirnach AG, Sirnach, Switzerland) installed using direct push techniques were used to observe the static and dynamic in situ pore pressure responses. The fabrication, calibration, and installation procedures have been discussed by Jana et al. (2021) and Jana (2021).

OSU Blast Array

Particle velocities measured at the nodes of the instrumentation elements formed by the geometry of the TGPs were used to determine shear strains within a given element through application of the numerical methods developed for finite-element analyses (FEA) (Chang et al. 2007; Cox et al. 2009; Roberts et al. 2016). PPTs placed in the center of the elements provide the u_e response corresponding to the strains imposed at the midpoint of each finite element. The novel geometry of the OSU Blast Array was designed to formulate three solid elements at different depths in order compute the dynamic 3D strain tensor during horizontal shaking applied using T-Rex and loading due to controlled blasting. Because near-field blast pulses produce three-dimensional body waves during the latter loading type, the solid element formulation was thought to provide a more accurate estimate of shear strain for charges located closest to the array. The 3D strain tensor was computed using the analytical formulation for 3D finite elements as described by Chandrupatla et al. (2002).

The TGPs and PPTs comprising the OSU Blast Array are shown in plan and elevation in Fig. 3 (compare with Figs. 1 and 2). The geometry of the sensor array was selected in consideration of several competing factors: (1) body wave velocities should be

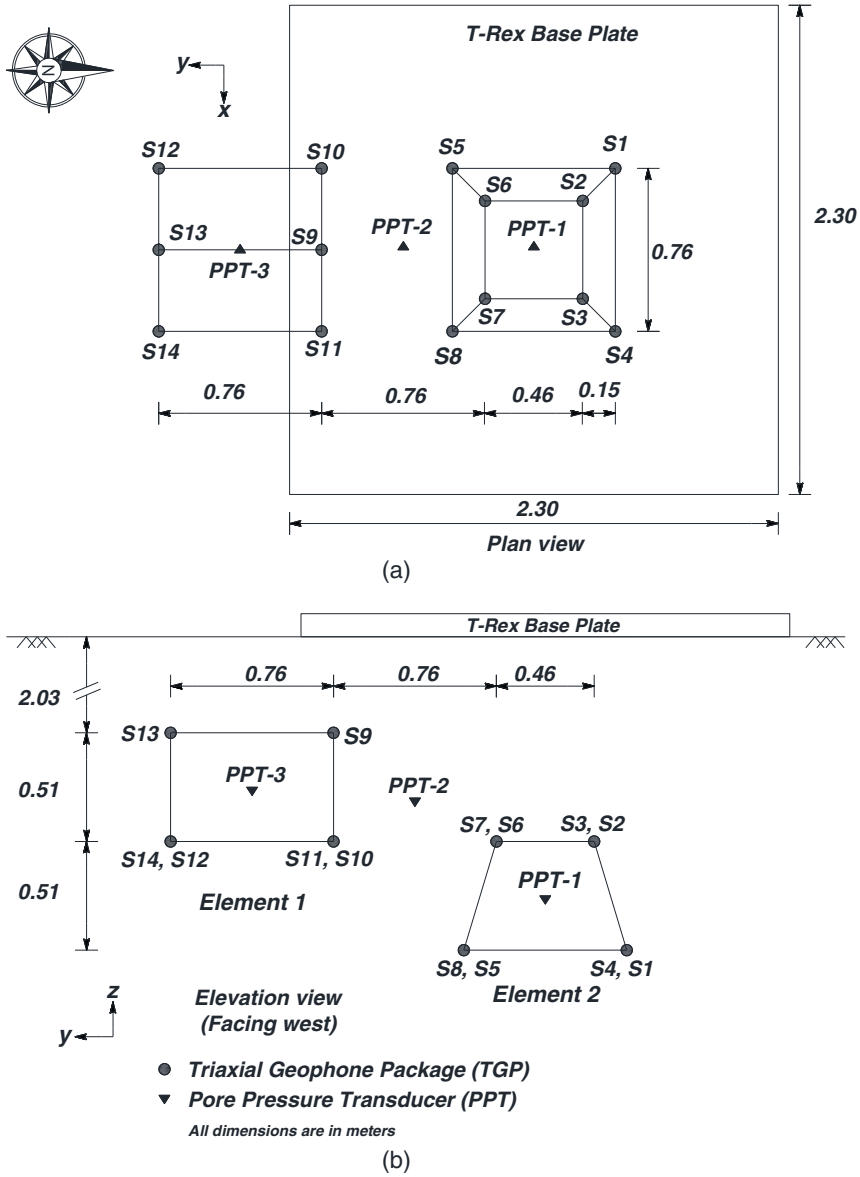

Fig. 3. Schematic of the instruments and elements comprising the OSU Blast Array: (a) plan view; and (b) elevation view (facing west), indicating the arrangement of the T-Rex base plate. Element 3, formed by TGPs S10, S9, S11, and S7, is not shown for clarity.

measured using separation distances less than or equal to one quarter of the anticipated wavelength of the shear waves (Cox 2006) considering their predominant frequency f and degradation in velocity during loading, (2) the soil inside the array must experience as little disturbance as possible, and therefore the TGPs should be as far apart as admissible, and (3) the TGPs should be installed in a sequence and pattern that minimizes disturbance. The vertical geophone in TGP S8 (i.e., TGP S8z) malfunctioned following installation; thus, two solid wedge elements formed by TGPs S9, S10, S11, S12, S13, and S14 (Element 1) and TGPs S1, S2, S3, S4, S5, and S6 (Element 2) (Fig. 3), were analyzed. A third tetrahedral array, Element 3 (formed by TGPs S10, S9, S11, and S7; not shown) was also analyzed for comparison with measurements made using PPT-2 (Fig. 3).

Dynamic Loading Programs Executed

Three sets of experiments were performed once the instrumented arrays were placed: (1) small-strain seismic downhole testing (before and after loading events), (2) staged shaking with T-Rex, and (3) controlled blasting. Due to the low-to-moderate magnitudes of strains imposed by T-Rex (i.e., 0.002% to 0.15% for the tests presented herein), T-Rex shaking was performed prior to controlled blasting. The base plate of T-Rex was centered over Element 2, aligned with the blast casing centerline (Fig. 1), and partially covered Element 1 (Fig. 3). The u_e generated due to the portion (200 kN) of the weight of the mobile shaker (284.4 kN) applied by the baseplate was monitored and allowed for calculation of the increment of effective stress applied at the locations of the PPTs. Once the u_e generated due to the placement of T-Rex dissipated, staged shaking commenced in the east–west direction (aligned with the blast casings) to produce maximum velocity amplitudes along the x component of each TGP (Figs. 1 and 3). Five shaking events were conducted using uniaxial sinusoidal motions that were applied for 4 s with $f = 10$ Hz; each loading stage was separated by the duration necessary for dissipation of the u_e generated in the previous loading stage.

The controlled blasting experiment required selection of the charge weights, depths, and locations, as well as the detonation sequence in view of the anticipated generation of body waves, which vary as a function of the geometry of the charge (e.g., small single-charge decks produce more spherical wavefronts, whereas multi-charge decks produce more cylindrical wavefronts). The theoretical radiation pattern of buried explosives suggests that *P*-waves mainly emanate in the radial direction, whereas shear waves, or *S*-waves, travel at an angle of approximately 45° relative to the longitudinal charge axis (Heelan 1953). The basis for the charge weights, locations, and detonation sequence conducted at the OSU Blast Array was informed by the blasting experiments performed at the Port of Portland, Oregon (Jana and Stuedlein 2021a, b), where deviations from the theoretical radiation patterns were observed. For example, the maximum blast-induced *P*-wave amplitude for the charges implemented in this and the previous study was horizontal, whereas the maximum *S*-wave amplitude was inclined in an envelope ranging from 15° to 35° from horizontal.

Twelve blast casings were installed to allow placement of charges: Casings C1 through C10 were placed in the east–west direction to provide a predominantly 2D waveform toward Elements 1 and 2 (Fig. 1), whereas Casings CX1 and CX2 were located north of the array and were fitted with small charges to ostensibly interrogate the small-strain shear-wave velocity within the array in between detonations of the larger charges, as described subsequently. Casings C1 through C10 were offset 0.92 m from the east–west centerline to minimize interference of the seismic waveforms traveling along the assumed linear ray path.

Forty-five explosive charges were detonated over a 30-s period, as illustrated in Fig. 4 and detailed in Table S1. The controlled blasting experiment started with small 90-g charges located 15.25 m from the center of Element 2, which were intended to generate a linear-elastic soil response. As the experiment proceeded, the charge weight increased as the distance to the array decreased to induce nonlinear-elastic, followed by nonlinear-inelastic, soil responses. Upon detonation of the largest charges (1.36 kg), the charge weights were reduced to maintain the integrity of the TGPs. Every third charge consisted of an interrogator charge detonated from casing CX-1 or CX-2 (Figs. 1 and 4) to generate an independent crosshole source for monitoring shear-wave velocity.

Computation of Shear Strain for the Solid (3D) Elements

The two solid (3D) wedge Elements 1 and 2 provided particle displacements at six nodes and were used along with the appropriate shape functions to obtain the 3D shear strain at the midpoint of each element in an extension of the 2D methodology implemented by Cox et al. (2009), Roberts et al. (2016), and Jana and Stuedlein (2021a, c). Full waveform particle velocities sampled at 10 kHz were measured at each TGP, integrated to provide particle displacements, and used to compute the corresponding shear strain time histories.

The stress paths arising from T-Rex shaking and blasting differ from those associated with various laboratory element tests, such as the direct simple shear (DSS) test. Although the particle motions produced by T-Rex shaking are predominantly horizontally polarized and vertically propagating, rocking of the T-Rex baseplate also generates some vertically polarized and vertically propagating particle motion, which was taken into account (e.g., Zhang 2020). Blast-induced particle motions are complex, and the predominant particle velocity is governed by the location of the energy source and the boundary conditions of the explosive (e.g., the length of the charge relative to the scale of the observation). The 3D instrumented array used in this study allowed the estimation of the six-component 3D Cauchy strain tensor using the finite-element formulation (Chandrupatla et al. 2002). To compare the maximum, mobilized in situ shear strain on a common basis with DSS tests, which are often used to simulate vertically propagating horizontally polarized S_{VH} waves, the DSS-equivalent shear strain (e.g., Cappa et al. 2017; Jana and Stuedlein 2021a, b), $\gamma_{DSS,eq}$, was computed for the T-Rex and blast-induced strains. The deviatoric strain invariant, or the octahedral shear strain, γ_{oct}, may be computed from the Cauchy strain tensor as follows (Chang 2011):

$$\gamma_{oct} = \left(\frac{2}{3}\right)\sqrt{(\varepsilon_{xx}-\varepsilon_{yy})^2+(\varepsilon_{yy}-\varepsilon_{zz})^2+(\varepsilon_{zz}-\varepsilon_{xx})^2+\frac{3}{2}(\gamma_{zx}^2+\gamma_{xy}^2+\gamma_{yz}^2)} \quad (1)$$

where ε_{xx}, ε_{yy}, and ε_{zz} = normal strains in the *x*-, *y*-, and *z*-directions; and γ_{zx}, γ_{xy}, and γ_{yz} = shear strain components of the 3D Cauchy strain tensor. The constant-volume $\gamma_{DSS,eq}$ can then be calculated as follows (Cappa et al. 2017):

$$\gamma_{DSS,eq} = \sqrt{\frac{3}{2}}\gamma_{oct} \quad (2)$$

by setting normal strains equal to zero. The use of Eq. (2) allows direct comparison of the in situ shear strains with those developed from laboratory DSS tests.

Overview of In Situ Dynamic Responses

T-Rex Shaking

The OSU Blast Array was subjected to T-Rex shaking on May 28, 2019. Loading of the instrumented array was applied in Stages 1 to 5 to produce incrementally increasing particle velocities and displacements, corresponding to average peak horizontal ground shear forces of 5, 24, 60, 83, and 106 kN. The maximum ground surface acceleration measured at the T-Rex baseplate was 2.04*g* during Stage 5. Shaking amplitudes varied spatially within the blast array, as observed below the center (Element 2) and sides (Element 1) of the T-Rex baseplate. Because the predominant amplitude of shaking occurred along the east–west direction, the maximum particle velocities within Elements 1 and 2 were registered in the *x*-component of TGPs, with smaller amplitudes in the *y*- and *z*-components (Figs. S2 and S3). Although the north–south or *y*-component of shaking was smaller than the vertical or *z*-component below the center of the baseplate (e.g., TGP S6) (Fig. S3), rocking or vertical motions were smaller than those of the *y*-component of TGP S9 (Element 1) (Fig. S2). The largest maximum particle velocity and displacement was 0.066 m/s and 1.16 mm, respectively, observed during Stage 5 in TGP S9x, away from the center of the baseplate. The preshaking and postshaking

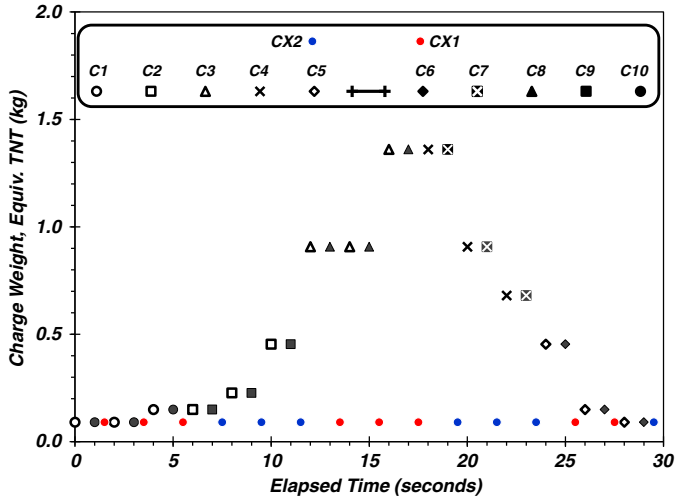

Fig. 4. Charge weight and detonation sequence conducted at the OSU Blast Array.

shear-wave velocities, particle velocities, and excess pore pressures corresponding to Stages 1 through 5 are publicly available from Stuedlein et al. (2021).

Fig. 5 presents the computed Cauchy shear strain γ in three orthogonal directions and the measured excess pore pressure ratio r_u time history for the five shaking events in Element 1. The maximum shear strain occurred in the zx plane due to the S_{VH} waves, dominated by the particle displacements in the x-direction (Fig. S2). Because the center of Element 1 was offset 0.23 m from the front edge of the baseplate (Fig. 3), intermediate shear strains were observed in the xy plane, whereas the smallest strains occurred in the yz plane. The first stage of loading did not generate residual excess pore pressure $u_{e,r}$ after 40 loading cycles, N, with $\gamma_{zx,\text{avg}}$ of 0.0017%, below the threshold shear strain γ_{tp} to trigger $u_{e,r}$ in plastic silt (Mortezaie and Vucetic 2016; Jana and Stuedlein 2021a, c). As the magnitude of the shear strain increased during the later stages of cyclic loading, the residual excess pore pressure ratio $r_{u,r} = u_{e,r}/\sigma'_{vc}$, defined as the excess pore pressure ratio at the end of each cycle (Dobry et al. 1982; Hsu and Vucetic 2006), increased because the shear strain in Stage 2 exceeded γ_{tp}. The maximum excess pore pressure ratio, $r_{u,\max}$ in Element 1 (observed using PPT-3) was 0.9% during Stage 2 with $N = 40$, to result in $r_{u,rN=40} = 0.4\%$ following loading, as a result of the maximum shear strain in the three orthogonal xy, yz, and zx planes of $\gamma_{xy,\max} = 0.0057\%$, $\gamma_{yz,\max} = 0.0019\%$, and $\gamma_{zx,\max} = 0.0186\%$, respectively. The maximum shear strains within Element 1 imposed by T-Rex shaking occurred during Stage 5, with $\gamma_{zx,\max} = 0.117\%$ which produced $r_{u,\max}$ and $r_{u,rN=40}$ of 18.4% and 16.5%, respectively.

Fig. 6 presents the shear strain and r_u time histories recorded in Element 2 (formed by TGPs S1, S2, S3, S4, S5, and S6) during the five shaking events. Similar to Element 1, the loading applied in Stage 2 exceeded γ_{tp}, in Element 2; as a result, $u_{e,r}$ developed during Stage 2 ($r_{u,r} = 0.27\%$ for $N = 40$) (Table 1). Because the T-Rex baseplate was centered over Element 2, $\gamma_{zx,\max}$ in Element 2 was greater than that of Element 1 for all five loading stages (Table 1). Moreover, Element 1 experienced greater horizontal shearing in the xy plane compared with Element 2 due to the eccentric location of Element 1 with respect to the T-Rex baseplate (Fig. 3).

The tetrahedral Element 3 (formed by TGPs S10, S9, S11, and S7) was also analyzed to enable the use of measurements made using PPT-2 (Fig. 3) with the 3D shear strain and r_u time histories presented in Fig. S4 for the five loading stages. The $r_{u,r}$ measured in Element 3 was larger than in Elements 1 and 2 (Table 1) for all loading events, and $r_{u,r}$ of 20% was observed after 40 cycles of loading for Stage 5. The larger u_e is attributed to multidirectional loading and potential pore pressure migration and trapping, as described subsequently.

Controlled Blasting Program

The OSU Blast Array was subjected to controlled blasting on May 29, 2019, following dissipation of T-Rex-induced $u_{e,r}$. Figs. 7(a–c) present example velocity time histories for three orthogonal components of three TGPs during the 30-s blasting program (Table S1). Particle velocities gradually increased during the progression of the blasting program as the charge weight increased and the blast source-to-sensor distance decreased. Several charges produced peak velocities exceeding 0.4 m/s, which are associated with the high-frequency P-waves (with f ranging from 1,000 to 1,666 Hz) due to their weight and the apparent alignment of the TGP with the most energetic portion of the radiation field. Figs. 7(d–f) present the waveforms generated due to Blasts 1, 28, and 37 measured using TGP S10 to demonstrate the components of blast-induced body waves. These include P-waves, followed by near-field longitudinally propagating (i.e., x-component dominant) vertically polarized shear waves, designated as SV_x-waves which are generated upon unloading of the P-wave (Jana and Stuedlein 2021b), and the far-field horizontally propagating vertically polarized (z-component dominant) shear waves, designated as SV_z-waves, generated at the locations of the charges. The frequencies of the near-field SV_x and far-field SV_z-waves ranged from 9 to 18 Hz [Figs. 7(d–f)] and fell within the range of earthquake ground motions.

The normalized Fourier amplitude spectra calculated by dividing the Fourier spectra of the particle velocity by its maximum Fourier amplitude are presented in Fig. S5(a) for the 45 individual blasts measured using TGP S4z. The results indicate an average predominant frequency of approximately 14 Hz. The average normalized Fourier amplitude spectra of the 41 individual TGPs and the global mean spectrum are presented in Fig. S5(b), which shows that the average predominant frequency of all of the blast-induced particle velocities ranged from 9.6 to 14.6 Hz. Low-frequency shear waves generated from the near- and far-field dominated the soil response. For example, Figs. 7(g–i) present examples of the particle displacements for TGP S10; the P-waves produced small displacement amplitudes in the soil owing to their very high frequencies (Jana and Stuedlein 2021a, b). Low-frequency near- and far-field shear waves produced large displacements, resulting in large shear strains, and generated shear-induced residual excess pore pressure.

The unloading of the P-wave produces shear strains that are small, which is followed by the near- and far-field shear wave–induced shear strain, either of which produced the maximum shear strain $\gamma_{\max}$ during a given blast pulse depending on the source-to-element distance, as observed in Blasts 1, 28, and 37 [Figs. 7(j–l)]. For the case of Blast 1, detonated far from the sensor array (15.25 m), the near-field shear wave arrived at 2.7014 s and produced $\gamma_{\max}$ without superposition of the far-field SV_z-wave-induced shear strain (time of arrival = 2.8341 s) [Fig. 7(j)]. Conversely, the near-element (i.e., ~3.18 m) Blast 37 exhibited superimposed near- and far-field shear waves [Fig. 7(l)], preventing identification of the component contributing most to $\gamma_{\max}$. Irrespective of the type of shear wave, shearing controls the soil response due to their low operative frequencies and correlates directly to the

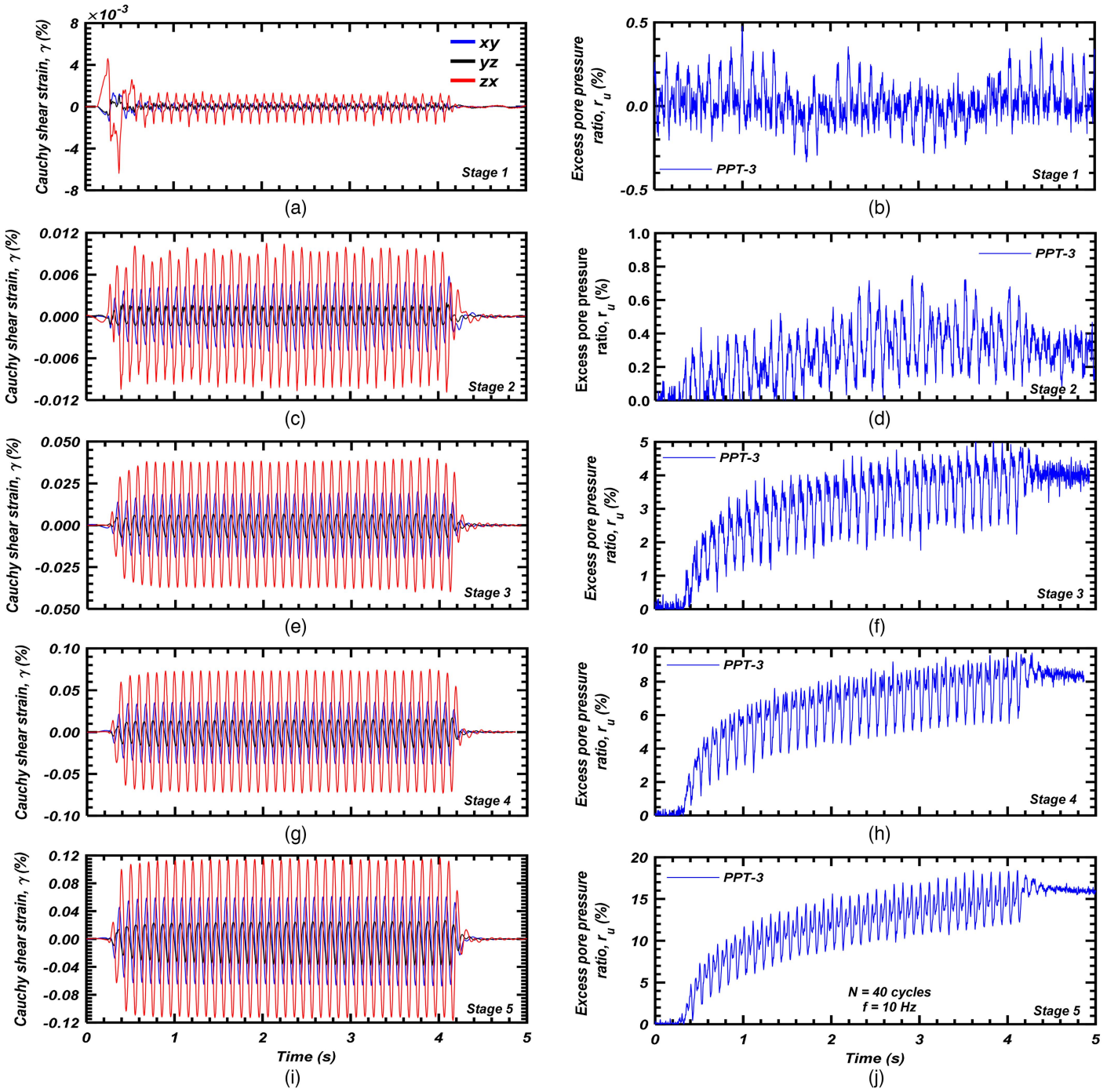

Fig. 5. Comparison of the calculated Cauchy shear strain and measured excess pore pressure ratio time histories in Element 1 during T-Rex shaking: (a and b) Stage 1; (c and d) Stage 2; (e and f) Stage 3; (g and h) Stage 4; and (i and j) Stage 5.

generation of u_e (Gohl et al. 2001; Jana and Stuedlein 2021a, b), as described subsequently.

Figs. 8(a and b) present the 3D Cauchy shear strain time histories for Elements 1 and 2 over the duration of the 30-s blasting sequence. The maximum Cauchy shear strain in xy, yz, and zx planes are 0.897%, 0.513%, and 0.794%, respectively, for Element 1, compared with 0.373%, 0.362%, and 0.391%, respectively, for Element 2. This observation is somewhat surprising given that the shallower Element 1 was placed south of the east–west centerline of the blast casings, suggesting that (1) the SV-wave amplitudes may not be symmetric in plan, (2) the variation in stratigraphy at the test site location influenced the azimuthal distribution of the SV-wave amplitude, and/or (3) P-wave-induced surface waves may have superimposed with the far-field SV-waves to amplify the registered particle velocity and displacement nearer to the surface. The predominant accumulation of shear strain in a given azimuthal bearing reverses in both elements over the course of the blasting program [Figs. 8(a and b)] due to differing charge weights detonating from differing depths and directions to result in the permanent accumulation of shear strain.

Figs. 8(c and d) illustrate the variation of $\gamma_{DSS,eq}$ and r_u for each element and their temporal correlation. The maximum DSS-equivalent shear strain $\gamma_{DSS,max}$ in Elements 1 and 2 was equal to 1.137% and 0.828% [Fig. 8(c)], respectively, whereas the

J. Geotech. Geoenviron. Eng., 2023, 149(3): 04023006

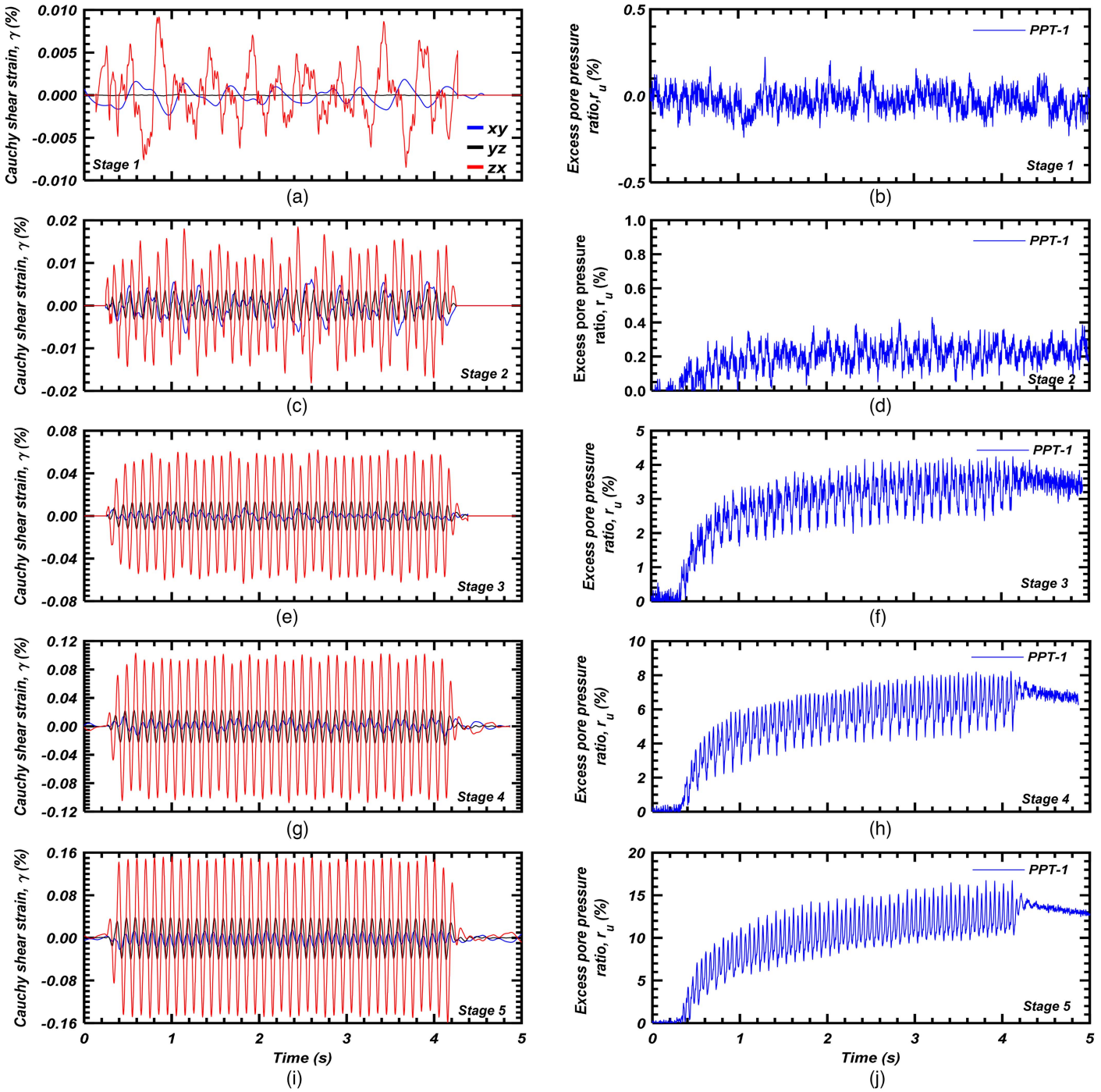

Fig. 6. Comparison of the calculated Cauchy shear strain and measured excess pore pressure ratio time histories in Element 2 during T-Rex shaking: (a and b) Stage 1; (c and d) Stage 2; (e and f) Stage 3; (g and h) Stage 4; and (i and j) Stage 5.

maximum shear-induced $r_{u,r}$ was approximately 61% and 55% for Elements 1 and 2, respectively [Fig. 8(d)]. The larger $\gamma_{DSS,max}$ in Element 1 resulted in the larger $r_{u,r}$. Differing from constant-volume or undrained shearing of laboratory test specimens, it is demonstrated in Fig. 8(d) that drainage occurred within the OSU Blast Array during shearing and that drainage tended to transiently inhibit or arrest the accumulation of shear strains. This coupled fluid-mechanical interaction is an important aspect of in situ testing: it provides a system response that obeys the existing field drainage conditions, which are unlikely to be captured in the laboratory. However, significant differences exist between the 3D excess pore pressure field generated by localized sources during in situ testing and the idealized one-dimensional (1D) conditions often assumed to represent seismic shaking (Jana and Stuedlein 2021b). Drainage was significantly greater in Element 2 than Element 1; the top quarter of Element 1 was situated in the high plasticity clayey silt to silty clay layer, with PPT-3 just below this layer (Figs. 2 and 3). The high plasticity layer acts to restrict or impede vertically migrating u_e.

Fig. 9 presents several examples of the $\gamma_{DSS,eq}$ and r_u time histories from the 30-s blasting program. The maximum shear strain and corresponding dynamic and residual excess pore pressures, defined as the magnitude of r_u following passage of the SV-wave and where no significant perturbations were measured

Table 1. Summary of the DSS-equivalent shear strain, number of cycles, and residual excess pore pressure ratio

Element	Shaking event stage	$\gamma_{xy,\max}$ (%)	$\gamma_{yz,\max}$ (%)	$\gamma_{zx,\max}$ (%)	$\gamma_{DSS,\max}$ (%)	$r_{u,r\,N=20}$ (%)	$r_{u,r\,N=30}$ (%)	$r_{u,r\,N=40}$ (%)	$r_{u,\max}$ (%)
1	1	0.0005	0.0003	0.0017	0.0019	0.00	0.00	0.00	0.00
	2	0.0057	0.0019	0.0186	0.0097	0.32	0.40	0.40	0.90
	3	0.0191	0.0114	0.0355	0.0391	3.36	3.76	4.12	5.10
	4	0.0402	0.0171	0.0751	0.0738	6.80	7.51	8.63	9.74
	5	0.0373	0.0677	0.1167	0.1166	12.12	14.10	16.51	18.39
2	1	0.0000	0.0000	0.0018	0.0020	0.00	0.00	0.00	0.00
	2	0.0070	0.0036	0.0185	0.0145	0.23	0.27	0.27	0.48
	3	0.0060	0.0145	0.0630	0.0557	3.13	3.51	3.65	4.23
	4	0.0135	0.0271	0.1046	0.1001	6.08	6.67	7.57	8.20
	5	0.0291	0.0417	0.1490	0.1497	11.62	12.70	14.05	16.71
3	1	0.0019	0.0020	0.0017	0.0017	0.00	0.00	0.00	0.00
	2	0.0097	0.0145	0.0123	0.0123	0.39	0.45	0.49	0.93
	3	0.0145	0.0237	0.0402	0.0410	4.35	4.74	5.35	6.18
	4	0.0232	0.0437	0.1189	0.0805	6.88	8.30	11.02	12.53
	5	0.0382	0.0796	0.1237	0.1291	13.79	16.95	19.95	23.09

(Jana and Stuedlein 2021a, b), became progressively larger as the charge weight increased and/or was detonated closer to the array (Fig. 4). The r_u time histories indicate the transient high-frequency P-wave-induced u_e followed by shear-induced u_e. The frequency of the P-wave is too great to cause $u_{e,r}$ because P-waves of such frequencies pass in a drained elastic state (Ishihara 1968). During Blast 16, $\gamma_{DSS,\max} = 0.067\%$ and 0.041% in Elements 1 and 2, respectively, and the corresponding $r_{u,r}$ was 3.1% and 2.6%, respectively [Figs. 9(a and b)].

As the blasting program progressed, large magnitudes of shear strain developed in the soil resulting in high $r_{u,r}$. For example, during Blast 37, $\gamma_{DSS,\max} = 0.885\%$ and 0.802% in Elements 1 and 2, respectively, and the corresponding $r_{u,r}$ was equal to 55.5% and 43.4%, respectively [Figs. 9(c and d)]. The direct temporal relationship between the independently obtained time-varying γ_{DSS} and r_u is evident. The preblasting and postblasting shear-wave velocities, particle velocities, and excess pore pressures corresponding to the controlled blasting experiment are publicly available from Stuedlein et al. (2021).

Variation of Excess Pore Pressure with Shear Strain

Response to T-Rex Shaking

The constant-volume $\gamma_{DSS,eq}$ was calculated using γ_{oct} [Eqs. (1) and (2)] for the five T-Rex shaking stages to develop the relationship between $\gamma_{DSS,\max}$ and $r_{u,r}$ for Elements 1, 2, and 3 for various numbers of cycles, N [Fig. 10(a)]. The $\gamma_{DSS,\max}$ in the three elements was $\leq 0.002\%$ during Stage 1 shaking and did not trigger $r_{u,r}$ because γ_{tp} was not exceeded. However, the OSU Blast Array exceeded γ_{tp} under Stage 2 loading, with $r_{u,r\,N=40}$ equal to 0.40%, 0.27%, and 0.61%, corresponding to $\gamma_{DSS,\max}$ equal to 0.0097%, 0.0145%, and 0.0123% for Elements 1, 2, and 3, respectively. The γ_{tp} separates nonlinear elasticity from nonlinear inelasticity (marked by the generation of u_e) and is therefore defined as the largest shear strain amplitude for which cyclic (or dynamic) loading will not result in the generation of excess pore pressure (Dobry et al. 1982). Due to the accuracy and precision of pore pressure measurements in the field and laboratory, some small nonzero $r_{u,r}$ is generally attributed to γ_{tp} or extrapolation to zero $r_{u,r}$ is performed to estimate γ_{tp} (Dobry et al. 1982; Mortezaie and Vucetic 2016). The γ_{tp} for Elements 1, 2, and 3 was estimated equal to 0.007%, 0.011%, and 0.010%, respectively, and represents the initial state of the silt deposit.

The magnitude of $r_{u,r}$ in Elements 1 and 3 was greater than that of Element 2 during all five stages of dynamic loading (Table 1). This observation might be due to several possible mechanisms, such as the effect of multidirectional loading (Kammerer et al. 2002; Matsuda et al. 2013; Dobry and Abdoun 2015), spatial variability of the silt (Bong and Stuedlein 2018; Beyzaei et al. 2018, 2020) evident within the OSU Blast Array (Fig. S1), and/or corresponding migration of u_e (Cubrinovski et al. 2019; Jana and Stuedlein 2021a, b) during in situ testing. For example, the average q_t nearest Elements 1 (i.e., CPT-3) and 2 (i.e., CPT-2) was 0.84 (and 1.02, excluding the high-plasticity portion) and 0.67 MPa, respectively, and the corresponding average I_c was 2.76 (and 2.55, excluding the high-plasticity portion) and 2.83, respectively. Based on the q_t best representing each element, the soil within Element 1 was initially stiffer than that of Element 2; however, Element 1 is capped by the high-plasticity layer. Thus, the higher $r_{u,r}$ in Elements 1 and 3 could be attributed to the enhanced multidirectional loading and excess pore pressure migration (Element 2) and/or trapping (Element 1). The u_e generated during the positioning of T-Rex over the silt array was maximum in PPT-2 (Element 3), followed by PPT-3 (Element 1) and PPT-1 (Element 2), which was similar to the generation and dissipation of u_e observed in the dynamic loading scenario (Fig. S6). The u_e responses indicate that multidirectional seismic shaking is not the sole factor for the different dynamic responses that were observed. Rather, variability in soil properties and pore-pressure migration/trapping represent additional contributing factors (Fiegel and Kutter 1994; Beyzaei et al. 2018, 2020; Cubrinovski et al. 2019).

Response to Controlled Blasting

The variation of $\gamma_{DSS,\max}$ with $r_{u,r}$ observed during the 30-sec blasting program for all charges (i.e., main and interrogator charges) is presented in Fig. 10(b). The $\gamma_{DSS,\max}$ and $r_{u,r}$ shown in Fig. 10(b) are not associated with a particular number of strain cycles [e.g., T-Rex loading shown in Fig. 10(a)]. Rather, the $r_{u,r}$ developed following each blast pulse and the associated $\gamma_{DSS,\max}$ is paired to identify how a given strain excursion is related to the generation of excess pore pressure, following the independently-developed approaches of Jana and Stuedlein (2021a, b) and Kishida and Tsai (2021). The γ_{tp} for Elements 1 and 2 was estimated equal to 0.0097% and 0.0092%, respectively, from the blasting experiment (n.b., the blast-induced waveforms were not judged to be accurately resolved for the shape functions of Element 3),

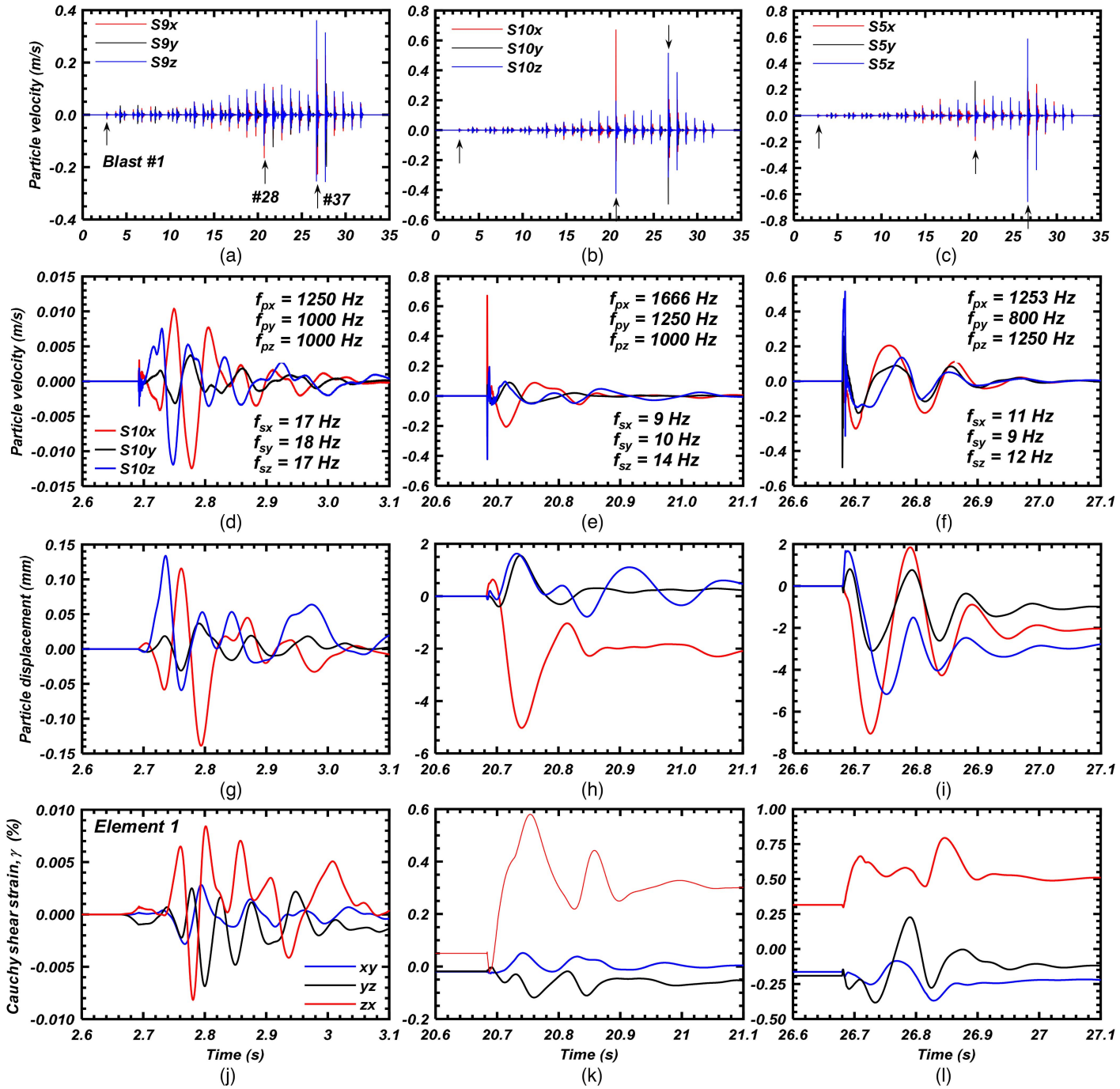

Fig. 7. Example dynamic responses during the blast program, including three-component particle velocity time histories for (a) TGP S9; (b) TGP S10; (c) TGP S5; (d–f) particle velocity; and (g–i) displacement time histories measured at TGP S10 during (d and g) Blast 1; (e and h) Blast 28; and (f and i) Blast 37; and Cauchy shear strain histories of Element 1 during (j) Blast 1; (k) Blast 28; and (l) Blast 37.

representing an increase and decrease in γ_{tp} relative to the staged T-Rex loading, respectively. The changes in γ_{tp} are attributed to changes in the soil fabric following T-Rex shaking as described in the last section of this paper. The smallest γ_{DSS} derived from blasting program was 0.0125%, which exceeded γ_{tp}, indicating that the first few charges should have been placed further away from the array in order to capture the linear-elastic response of the silt. The strain cycle–independent relationship between $\gamma_{DSS,max}$ and $r_{u,r}$ may be justified in view of the measured excess pore pressures (PPT-P5) and the average maximum shear strains at a depth of 2.9 m in the silty sand deposit at the Wildlife site during the 1987 Superstition Hills earthquake, as reported by Zeghal and Elgamal (1994). Fig. 10(b) presents the variation of the sequentially-increasing average γ_{max} (corresponding to assumed vertically propagating horizontally polarized shear waves, which are consistent with the DSS stress path) with the corresponding coincident measured r_u for the silty sand deposit. The agreement between the low-plasticity silt subjected to blast-induced ground motions studied herein and the Wildlife deposit subjected to earthquake ground motions is evident. Kishida and Tsai (2021) likewise demonstrate the link between γ_{max} and generation of excess pore pressures during seismic loading.

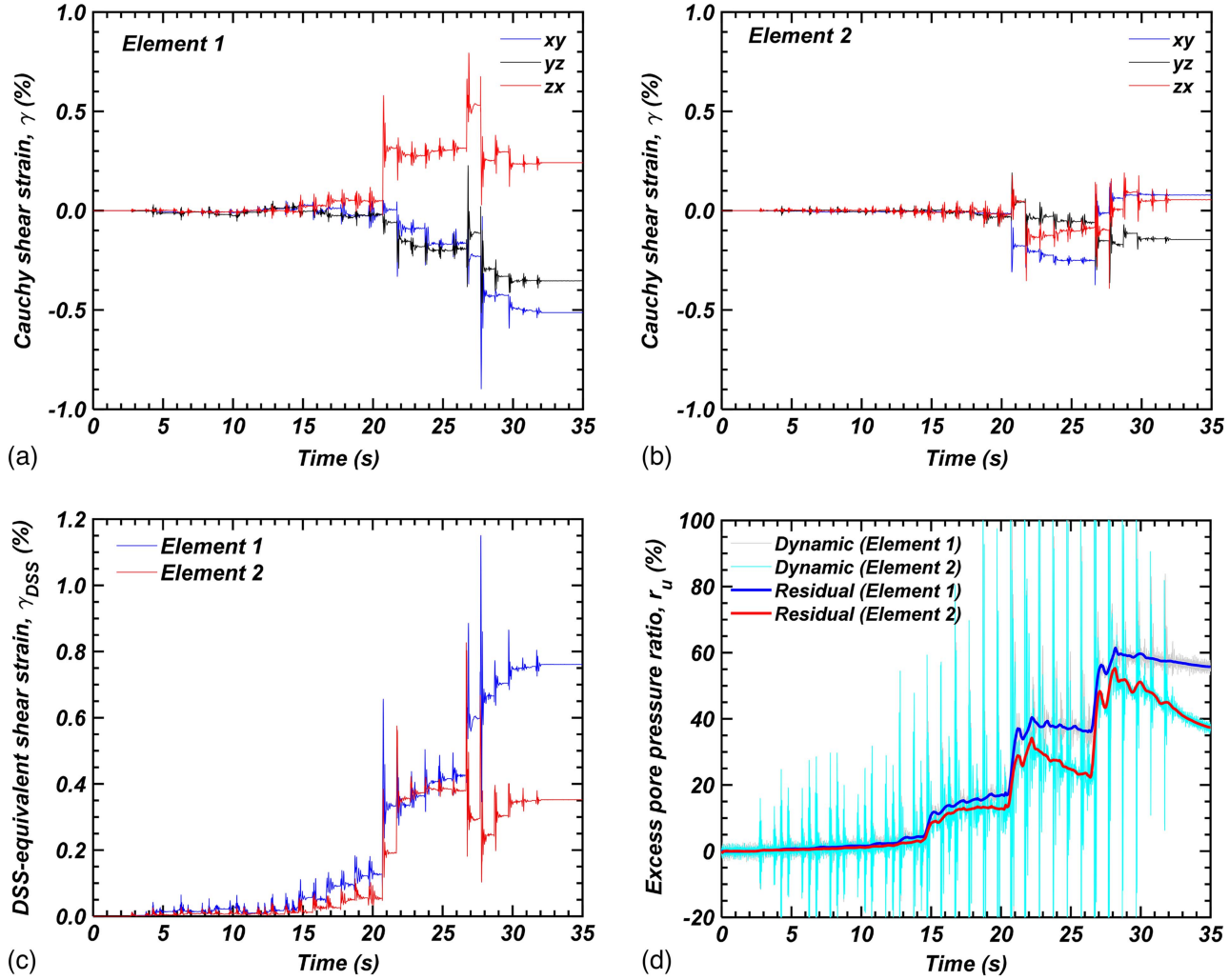

Fig. 8. Comparison of the calculated 3D Cauchy shear strain time histories for (a) Element 1; (b) Element 2; (c) corresponding DSS-equivalent shear strain time histories; and (d) measured dynamic and residual excess pore pressure ratio time histories for Elements 1 (PPT-3) and 2 (PPT-1) during the blasting program.

The $\gamma_{DSS,max}$–$r_{u,r}$ relationship derived from controlled blasting is well-bounded by the $N = 5$ and $N = 40$ relationships developed using T-Rex shaking for the shared range in strain imposed, demonstrating that the proposed controlled blasting technique can generally replicate the nonlinear-inelastic response from the highly controlled T-Rex shaking loading protocol. The $\gamma_{DSS,max}$ derived from the T-Rex shaking was 0.149%, with a corresponding $r_{u,r}$ of 14% after $N = 40$; in comparison, $\gamma_{DSS,max}$ imposed by the blasting program was 1.137% with a corresponding $r_{u,r}$ of 61%. The comparison of the u_e response further demonstrates the effectiveness of the controlled blasting technique to develop in situ dynamic soil responses over large ranges in strain.

Variation of Shear Modulus with Shear Strain

Shear-Wave Velocity Measurements during the T-Rex Loading Program

Downhole tests were conducted to determine the preloading and postloading small-strain V_s within the instrumented array when T-Rex was in position. Significant variability in the small strain V_s values were noted (Fig. S1) because each hammer strike can produce a different predominant frequency. This difference is attributed to the different wavelengths of the propagating S_{VH}-wave, which samples different volumes of the soil mass (Cox 2006). The average initial small-strain V_s in Elements 1 and 2 varied from 82 to 102 and 73 to 103 m/s, respectively, indicating the variability in the stiffness of the soil deposit within the instrumented array (Fig. S1 and Table S2).

Spectral analyses of body waves (SABW) and cross-correlation techniques (Kim 2012) were used to determine the nonlinear-elastic ($\gamma_{te} < \gamma < \gamma_{tp}$) to nonlinear-inelastic (i.e., $\gamma > \gamma_{tp}$), shear-strain-dependent V_s (Kishida et al. 2020; Kishida and Tsai 2021) during each cycle of T-Rex shaking using the horizontal velocities of two vertically separated geophones. Fig. S7 presents examples of the calculated variation of shear strain-dependent V_s in the array for several stages of shaking. The linear-elastic or small-strain V_s can be computed from the initial increasing ramp of the T-Rex loading level. For the case of TGPs S1*x* and S2*x* (Element 2), Stage 1 produced an average $\gamma_{DSS,max} = 0.002\%$ and corresponding strain-dependent $V_s = 94$ m/s which was less than the initial small-strain $V_s = 97$ m/s, indicating a nonlinear-elastic soil response. Following the Stage 1 shaking, the small-strain V_s increased, which is attributed to the effect of the prior strain history in the soil,

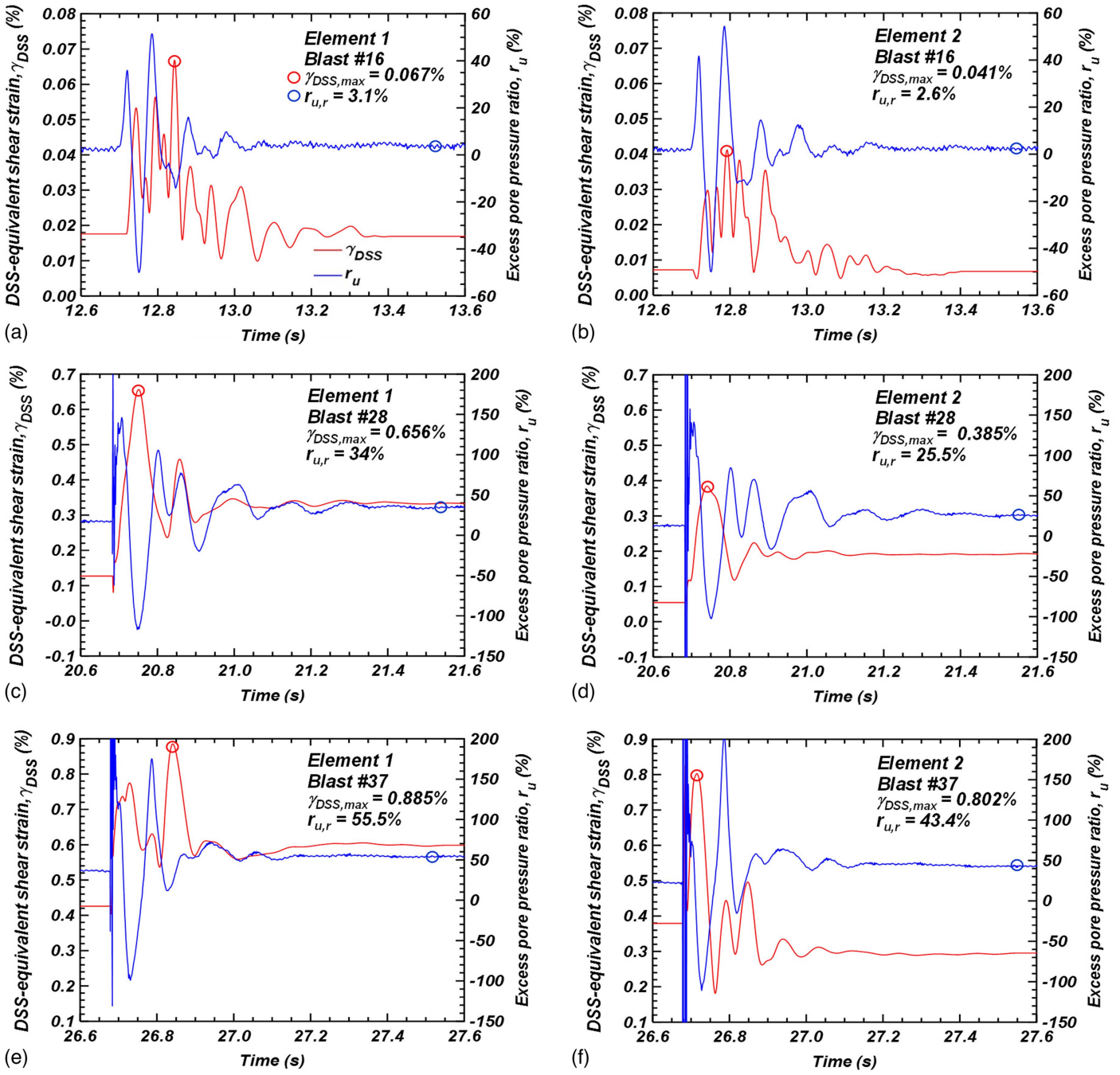

Fig. 9. Examples of (a, c, and e) DSS-equivalent shear strain; and (b, d, and f) excess pore pressure time histories; identification of $\gamma_{DSS,max}$ and $r_{u,r}$ for Elements 1 and 2 for (a and b) Blast 16; (c and d) Blast 28; and (e and f) Blast 37.

described in the section "Effect of Loading Stages and Strain History on the In Situ Dynamic Soil Response."

Shear-Wave Velocities in the Controlled Blasting Program

Downhole tests were conducted on the morning of May 29, 2019, to determine the preblast small-strain V_s within the OSU Blast Array (Table S3). These V_s values are used to provide the baseline soil stiffness. The average V_s derived from downhole tests prior to T-Rex shaking for Elements 1 and 2 was 94 and 90 m/s, respectively. The average V_s values derived from downhole testing prior to blasting were 98 and 94 m/s for Elements 1 and 2, respectively; the slight increase may be attributed to densification following T-Rex shaking. Examples of the blast-induced far-field SV_z-waves (i.e., S_{HV}-waves) that were measured in two horizontally-separated locations are presented in Fig. 11 and were used to track the evolution in the crosshole V_s during the blasting program and corresponding shear modulus, G. Jana et al. (2021) has given details on the computation of crosshole V_s from blast-induced body waves.

The shear-wave velocity reduced as the shear strain increased during the blasting program. Blast 1 produced a $\gamma_{DSS,max} = 0.124\%$ in Element 1 which was associated with a strain-dependent $V_s = 75$ m/s in TGPs S12z and S14z, exceeding both the linear-elastic and nonlinear-inelastic threshold shear strains γ_{te}, and γ_{tp}

J. Geotech. Geoenviron. Eng., 2023, 149(3): 04023006

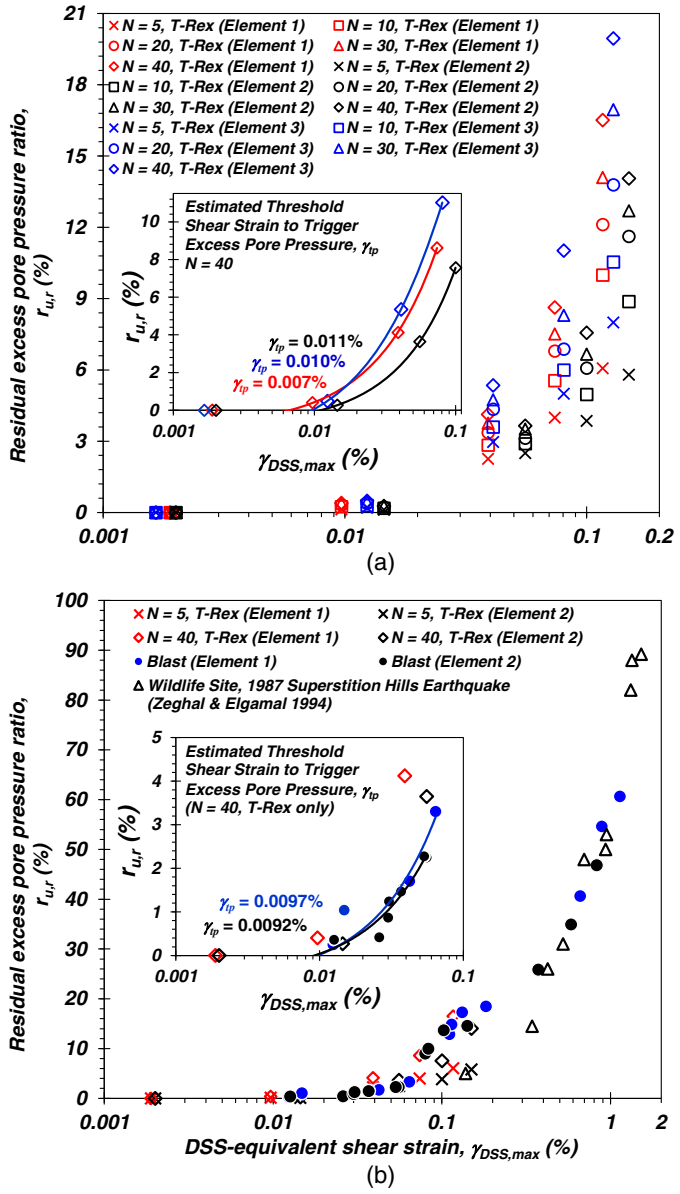

Fig. 10. Dynamic response of the instrumented silt deposit in terms of residual excess pore pressure ratio and maximum DSS-equivalent shear strain observed during (a) T-Rex shaking; and (b) comparison of T-Rex shaking–induced and blast-induced responses to the earthquake-induced response of the silty sand deposit at the Wildlife site (data from Zeghal and Elgamal 1994).

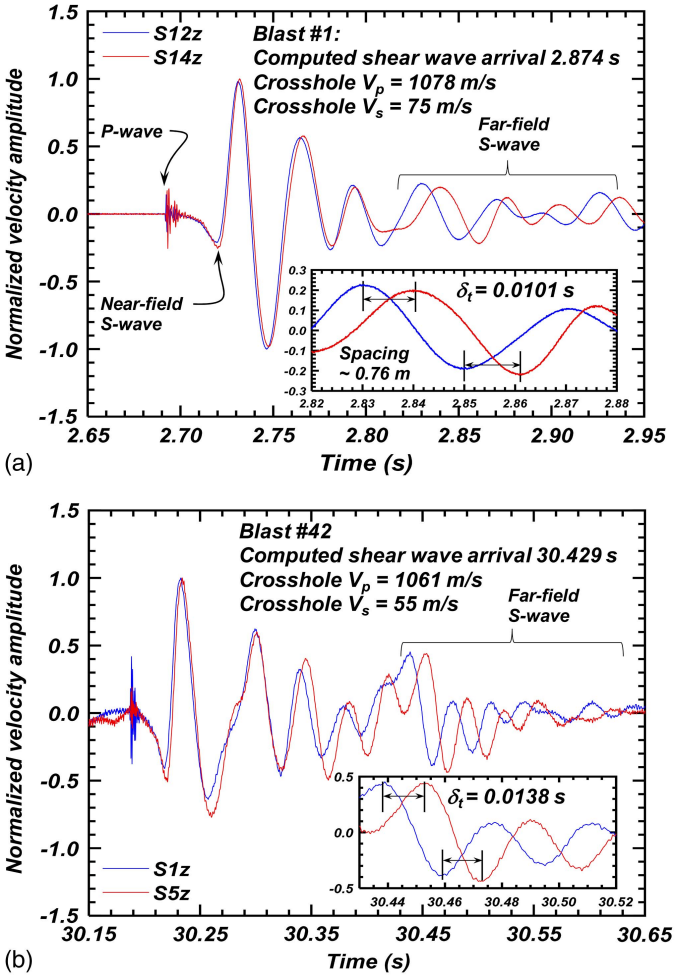

Fig. 11. Comparison of the SV-wave amplitudes and phases measured within two horizontally separated geophones: (a) TGPs 12z and 14z in Element 1, Blast 1; and (b) TGPs 1z and 5z in Element 2, Blast 42.

[Fig. 11(a)]. Blast 20 produced a $\gamma_{\mathrm{DSS,max}} = 0.114\%$ in Element 1 and the corresponding strain-dependent $V_s = 53$ m/s in TGPs S12z and S14z. The large reduction in V_s was attributed to the large shear strain imposed and the corresponding $r_{u,r}$. In Element 2, Blast 3 produced a $\gamma_{\mathrm{DSS,max}} = 0.026\%$ with a corresponding strain-dependent $V_s = 94$ m/s in TGPs S1z and S5z. In the same TGP pair, Blast 42 generated $\gamma_{\mathrm{DSS,max}} = 0.412\%$ and corresponding strain-dependent $V_s = 55$ m/s [Fig. 11(b)].

Shear Modulus Nonlinearity and Degradation

The shear strain–dependent V_s measured in the OSU Blast Array was used, along with the density of the silt, equal to 1,550 kg/m^3, to construct the normalized nonlinear shear modulus G/G_{max} variation with shear strain presented in Fig. 12(a). Because downhole tests were not available prior to every stage of T-Rex shaking, the particle velocity measured during the initial ramp loading (e.g., Figs. S2 and S3, and Cycle 0 in Fig. S7) was used to compute the small-strain V_s for each stage to provide a common basis for normalization to G_{max} because the wavelengths associated with downhole and T-Rex shaking, and therefore the volume of soil sampled, are different (Cox 2006). Because the first charge detonated exceeded γ_{te}, preblast downhole tests (summarized in Table S3) were used as the basis for normalization of the strain-dependent V_s for the blast-induced waveforms.

The independently-derived strain-dependent G/G_{max} results derived from the two distinct in situ testing techniques produced good agreement, considering the scatter resulting from both soil variability and differing wavelengths, as described previously. Fig. 12(a) shows that the in situ γ_{te} appears to vary from about 0.001% to 0.002%, which is similar to the range reported from previous laboratory studies (e.g., Vucetic and Dobry 1991; Stokoe et al. 1995; Darendeli 2001), and somewhat smaller than that observed (i.e., 0.002% to 0.003%) using blasting techniques in a silt deposit with PI = 28 reported by Jana and Stuedlein (2021a), consistent with the known role of plasticity on increased linearity of soils. Current and previous in situ test studies (Cox et al. 2009; Sahadewa et al. 2015; Jana and Stuedlein 2021a) showed that

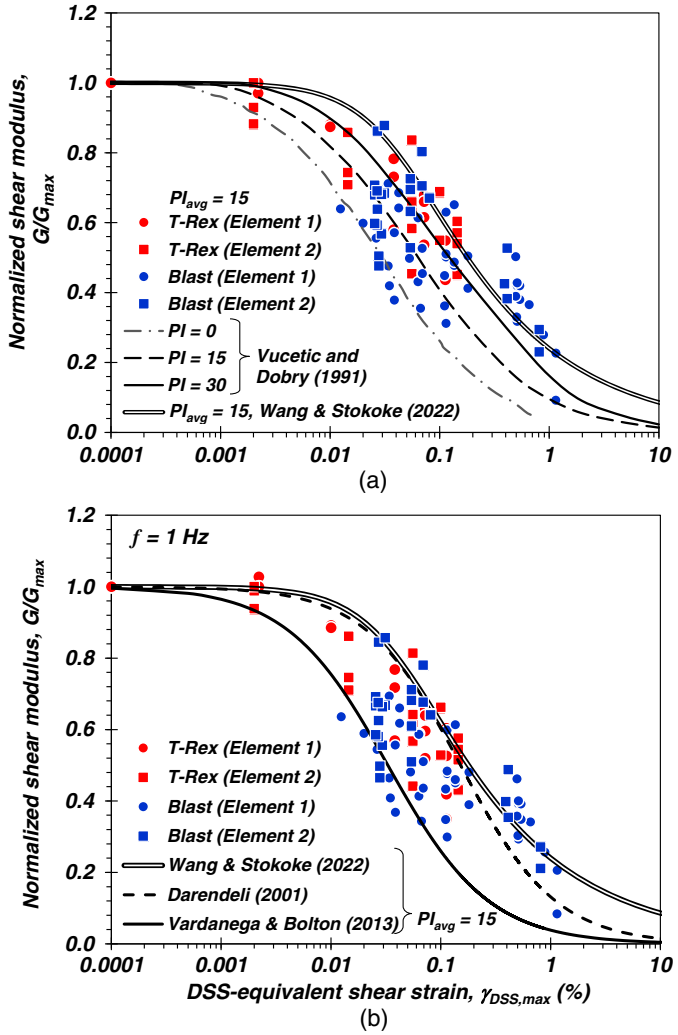

Fig. 12. Comparison of in situ normalized shear modulus nonlinearity with maximum DSS-equivalent shear strain derived from T-Rex shaking and controlled blasting: (a) without strain rate correction; and (b) with strain rate correction.

dynamic in situ tests can capture the appropriate constitutive threshold separating linear and nonlinear elasticity. Fig. 12(a) also shows that as shear strains increased, the shear modulus reduced to ~$0.9G_{max}$ at $\gamma_{DSS,max} \approx \gamma_{tp}$, whereas by $\gamma_{DSS,max} \approx 1\%$, the in situ shear modulus reduced further to ~0.1 to $0.3G_{max}$ corresponding to $r_{u,r}$ of ~60%.

The in situ test results generally compare well to, and exhibit slightly greater linearity than, the PI-dependent shear modulus reduction curves for plastic soil proposed by Vucetic and Dobry (1991), considering the scatter in the triaxial, direct simple shear, and resonant column tests forming the data set used to develop those curves. However, the data set comprising the Vucetic and Dobry (1991) curves represent a wide range in loading frequencies. The G/G_{max}-γ relationship depends on the strain rate (Isenhower and Stokoe 1981; Vucetic and Tabata 2003; Yniesta and Janati-Idrissi 2021) and can be corrected to a common frequency. The frequency of loading with T-Rex was 10 Hz, whereas the average and range in f of the blast-induced shear waves was 14 Hz, and $f_{min} = 6$ Hz to $f_{max} = 23$ Hz. The in situ G/G_{max}-γ data were therefore corrected to the common earthquake $f = 1$ Hz assuming a strain rate correction on G of 5% per $\log_{10}$ cycle proposed by Vardanega and Bolton (2013).

Fig. 12(b) presents the strain rate–corrected in situ G/G_{max}-γ data set for the instrumented silt deposit and compares it to the frequency-dependent Darendeli (2001), Vardanega and Bolton (2013), and frequency-independent Wang and Stokoe (2022) curves for $f = 1$ Hz and average PI = 15. Whereas some shear modulus nonlinearity and degradation curves only considered PI as the primary governing factor to determine the shape of the curves (i.e., Vucetic and Dobry 1991; Vardanega and Bolton 2013), Wang and Stokoe (2022) recently derived a two-parameter modified hyperbolic model to improve the representation of the G/G_{max}-γ relationship. The hyperbolic model requires void ratio, e, OCR, PI, FC, and the mean effective confining stress of the soil under consideration. The model provides a good upper-bound estimate of the in situ test data, in contrast to the Vardanega and Bolton (2013) model, whereas the Darendeli (2001) model agrees with the Wang and Stokoe (2022) model for $\gamma \leq 0.25\%$, after which a softer shear modulus occurs in the Darendeli model.

The laboratory test–derived curves indicated a greater reduction in G due to purely undrained and/or constant volume boundary conditions; drainage initating at large strains during the in situ tests led to a smaller rate of reduction in G/G_{max}. Whether drainage would occur in a similar manner at this site during an earthquake is unknown, and is complicated by the 3D excess pore pressure field induced by the local detonation of explosive charges versus the near-1D pore pressure field that is likely to occur during earthquake-induced shaking (Jana and Stuedlein 2021b).

Effect of Loading Stages and Strain History on the In Situ Dynamic Soil Response

The effect of each loading stage, including prestraining and large straining, on the dynamic response of the silt deposit was assessed using the average V_s calculated for each element prior to and following each loading stage after dissipation of u_e. Similar to the generation of G/G_{max} curves, the initial ramp loading was used to calculate the small-strain V_s for each T-Rex shaking stage. Figs. 13(a and b) present the variation of $\gamma_{DSS,max}$ and $r_{u,r}$ achieved during each dynamic loading event. The increase in the small-strain V_s relative to the initial V_s, $V_{s,i}$, prior to Stage 2 of T-Rex loading is $V_s/V_{s,i} = 1.01$ and 1.15 for Elements 1 and 2, respectively. This increase in V_s is attributed to the effect of the prior, limited strain history in the soil (Finn et al. 1970; El-Sekelly et al. 2017; Dadashiserej et al. 2022a) [Figs. 13(c and d)], which is thought to remove some local metastable soil grain contacts and increase the lateral stresses in the strained mass. However, as the magnitude of γ increased, the soil fabric became damaged, which resulted in a notable reduction in soil stiffness in Element 1.

For example, Stage 2 of T-Rex loading produced $\gamma_{DSS,max} = 0.0097\%$ and 0.0145% and corresponding $r_{u,r} = 4.12\%$ and 3.65% in Elements 1 and 2, respectively, with a postdissipation reduction in V_s from 127 to 112 m/s or $V_s/V_{s,i} = 0.89$ in Element 1. In contrast, $V_s/V_{s,i}$ in Element 2 increased from 1.15 following Stage 1 to 1.17. Following the Stage 3 loading, V_s reduced in both Elements 1 and 2 relative to Stage 2, and relative to the initial conditions for Element 1 (i.e., $V_s/V_{s,i} = 0.81$ and 1.10 for Elements 1 and 2, respectively). The effect of destruction of the soil fabric was more predominant than the effect of densification due to dissipation of $r_{u,r}$, particularly for Element 1. Continued increases in the strain amplitude associated with Stages 4 and 5 led to continued decreases in $V_s/V_{s,i}$ for Element 1, which exhibited slightly larger $r_{u,r}$, and little further change in the deeper Element 2, despite the slightly larger strain amplitudes generated in Element 2.

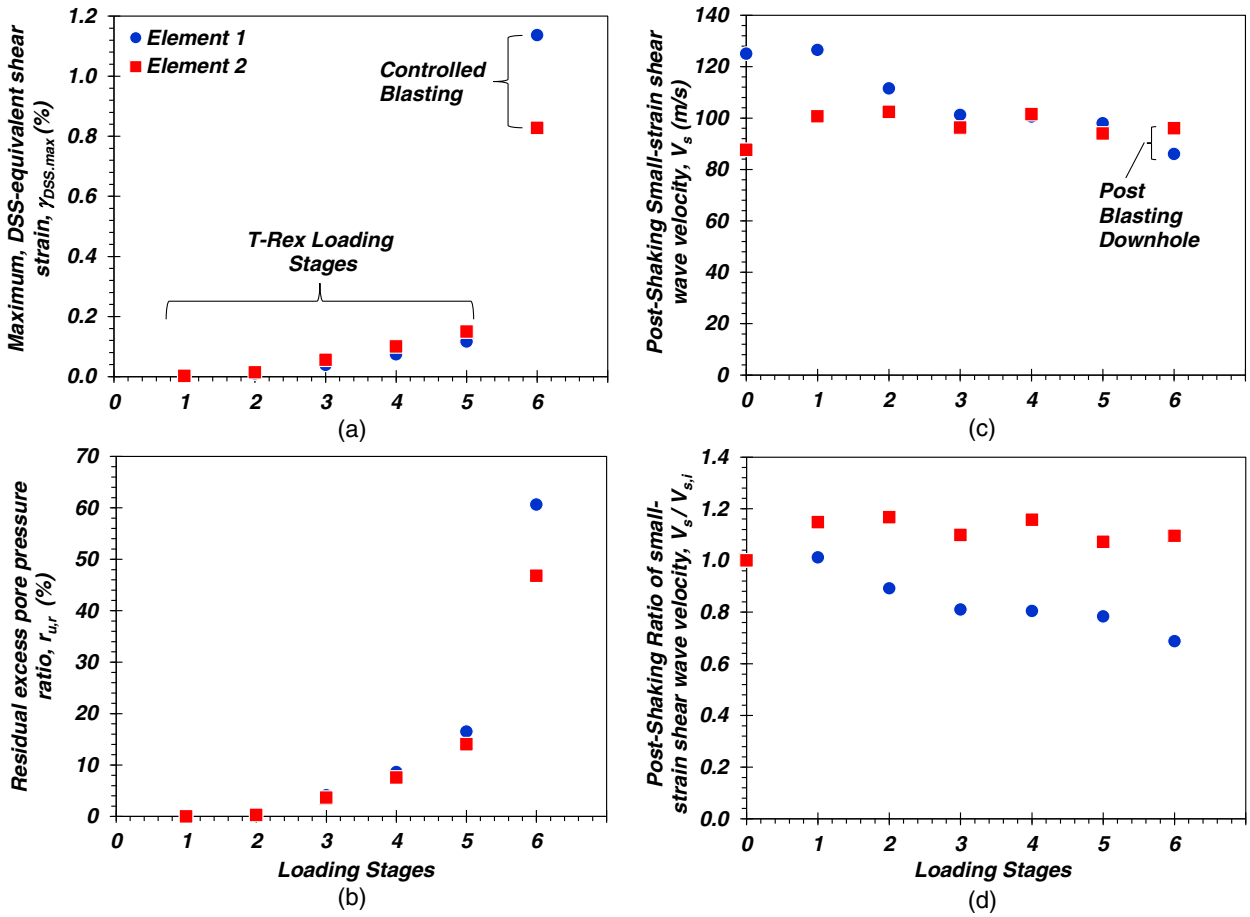

Fig. 13. Effect of prestraining and large-straining on the in situ dynamic response of the silt within the OSU Blast Array: (a) T-Rex shaking–induced and controlled blast-induced maximum DSS-equivalent shear strain amplitudes for mild and large loading stages; variation of (b) maximum residual excess pore pressure ratio; (c) shear-wave velocity; and (d) ratio of V_s with the initial V_s prior to Stage 1 loading for each loading stage.

The small-strain downhole V_s prior to controlled blasting was 98 and 94 m/s for Elements 1 and 2, respectively. During the blasting program, the silt experienced large shear strains and $r_{u,r}$ [Figs. 8 and 10(b)]. After full dissipation of u_e following the blasting program, $V_s = 86$ and 96 m/s for Elements 1 and 2, respectively. The large magnitude of shear strain in Element 1 caused significant further disturbance to the soil fabric, which had overcome the gain in stiffness due to densification from the dissipation of u_e following the prior dynamic event (Finn et al. 1970; Oda et al. 2001; Olson et al. 2001). On the other hand, V_s increased in Element 2 after controlled blasting. Although this might be attributable to the slightly lower $\gamma_{DSS,max}$ and $r_{u,r}$ (El-Sekelly et al. 2017; Dobry et al. 2019), the drainage in Element 2 during controlled blasting [Fig. 8(d)] likely contributed to the increase in densification and corresponding gain in soil resistance (Wang et al. 2019; Adamidis et al. 2019).

For example, Figs. 2 and S1 indicate subtle differences in the soil composition which may have contributed to the varying drainage behavior in Elements 1 and 2, with the majority of Element 1 capped by the drainage-restricting high-plasticity clayey silt to silty clay layer. Considering the differences in initial density and stiffness (e.g., q_t and V_s) (Figs. 2, 13, and S1) and the potential for impedance and/or restriction of drainage (e.g., Fiegel and Kutter 1994) [Fig. 8(d)], progressively increasing shaking intensities led to a decrease and increase in stiffness in Elements 1 and 2, respectively. The change in stiffness is supported by the changes in γ_{tp} (Fig. 10); γ_{tp} reduced from 0.011% to 0.0092% in Element 2 (corresponding to an increase in V_s), whereas γ_{tp} increased from 0.0070% to 0.0097% in Element 1, consistent with stiffness-driven behavior of the micromechanical model proposed by e.g., Dobry et al. (1982). These in situ dynamic tests clearly identified the changes in the nonlinear-inelastic soil constitutive response due to strain history and various drainage boundary conditions, which could serve to illuminate possible consequences for assessing the effects of aftershocks following a mainshock earthquake event (Dobry et al. 2019).

Summary and Conclusions

In this paper, a description of the first known effort to characterize and compare the in situ dynamic response of an instrumented silt deposit generated using two different methods: vibroseis shaking using the NHERI@UTEXAS mobile shaker T-Rex and the refined controlled blasting technique. These two distinct in situ testing techniques produced remarkably similar multidirectional dynamic nonlinear-inelastic responses over the shared range in shear strain, confirming the appropriateness of both methods and usefulness of the controlled blasting method. These experiments were facilitated through the use of novel instrumentation geometry, designed to formulate three in situ solid (3D) elements at different depths, which facilitated the computation of the 3D strain tensor from the two sources of dynamic loading. Five stages of shaking applied by the T-Rex shaker and one controlled blasting experiment produced

incrementally increasing 3D particle velocities, displacements, and corresponding shear strains γ. The following may be concluded based on the results of the field campaign:

- Stage 5 loading using the T-Rex mobile shaker produced the maximum DSS-equivalent shear strain $\gamma_{DSS,max}$ observed during T-Rex shaking and equal to 0.117%, 0.150%, and 0.129% for Elements 1, 2, and 3. These strains corresponded to residual excess pore pressure ratios $r_{u,r}$ of 16.5%, 14.1%, and 19.95%, respectively. Multidirectional (i.e., 3D) loading, spatial variability in the soil within the instrumented array, and migration and restricted drainage of excess pore pressures u_e contributed to the observed silt responses.
- The seismic energy generated from the 30-s controlled blasting program triggered the nonlinear-inelastic response in the soil. The predominant frequencies of the blast-induced particle velocities ranged from 9.6 to 14.6 Hz, which is in the range of earthquake-induced ground motions and similar to that provided by the vibroseis shaker (10 Hz).
- The frequencies of the blast-induced *P*-waves were too large to cause residual u_e because they passed in a drained elastic state. The low-frequency shear waves generated from the near- and far-field produced large displacements, resulting in large shear strains, and generated shear-induced residual u_e.
- The controlled blasting experiment produced an equivalent $\gamma_{DSS,max}$ of 1.137% and 0.828%, and generated corresponding maximum shear-induced $r_{u,r}$ of 61% and 55% for Elements 1 and 2, respectively.
- The threshold shear strain to develop residual excess pore pressure γ_{tp} estimated for Elements 1, 2, and 3 during T-Rex shaking was 0.007%, 0.011%, and 0.010%, respectively. During the controlled blasting event, γ_{tp} estimated for Element 1 increased to 0.0097% whereas that for Element 2 reduced to 0.0092%. These changes in γ_{tp} are attributed to the changes in soil fabric resulting from the prior large-strain history as demonstrated in Fig. 13, aided through pore pressure migration from Element 2 and impeded drainage in Element 1 [Fig. 8(d)].
- The two testing techniques demonstrated that the in-situ shear modulus, G, reduced to 90% of the maximum shear modulus, G_{max}, at $\gamma_{DSS,max} \approx \gamma_{tp}$, whereas by $\gamma_{DSS,max} \approx 1\%$, G further reduced to 10 to 30% of G_{max} corresponding to $r_{u,r}$ of ~60%.
- The Wang and Stokoe (2022) G/G_{max} model provided a good upper-bound estimate of the observed in situ G/G_{max}-γ behavior for the average silt plasticity index (equal to 15) for the instrumented deposit, whereas the frequency-independent Vucetic and Dobry (1991) and frequency-dependent Vardanega and Bolton (2013) models appear to provide an average and lower-bound estimates of the in situ G/G_{max}-γ behavior, respectively. Drainage during controlled blasting leads to higher G/G_{max} relative to that expected from constant-volume laboratory element tests.

Data Availability Statement

Some or all data, models, or code generated or used during the study are available in a repository or online with funder data retention policies. These data are available at Stuedlein et al. (2021).

Acknowledgments

The work described in this paper was funded by the National Science Foundation (NSF) under Grant Nos. CMMI 1663654, CMMI 1663531, and CMMI 1520808. The findings presented herein represent that of the authors and do not necessarily represent views of NSF. The authors express their gratitude to the Port of Longview, Longview, Washington, and their employees for providing and coordinating access to the test site.

Supplemental Materials

Tables S1–S3 and Figs. S1–S7 are available online in the ASCE Library (www.ascelibrary.org).

References

Adamidis, O., and S. P. G. Madabhushi. 2018. "Experimental investigation of drainage during earthquake-induced liquefaction." *Geotechnique* 68 (8): 655–665. https://doi.org/10.1680/jgeot.16.P.090.

Adamidis, O., U. Sinan, and I. Anastasopoulos. 2019. "Effects of partial drainage on the response of Hostun sand: An experimental investigation at element level." In Vol. 4 of *Earthquake geotechnical engineering for protection and development of environment and constructions*, 993–1000. Boca Raton, FL: CRC Press.

Andrus, R. D., N. P. Mohanan, P. Piratheepan, B. S. Ellis, and T. L. Holzer. 2007. "Predicting shear-wave velocity from cone penetration resistance." In *Proc., Earthquake Geotechnical Engineering, 4th Int. Conf. on Earthquake Geotechnical Engineering—Conf. Presentations CD-ROM*, edited by K. D. Pitilakis. Dordrecht, Netherlands: Springer.

Andrus, R. D., and K. H. Stokoe II. 2000. "Liquefaction resistance of soils from shear-wave velocity." *J. Geotech. Geoenviron. Eng.* 126 (11): 1015–1025. https://doi.org/10.1061/(ASCE)1090-0241(2000)126:11(1015).

Beyzaei, C. Z., J. D. Bray, M. Cubrinovski, S. Bastin, M. Stringer, M. Jacka, and R. Wentz. 2020. "Characterization of silty soil thin layering and groundwater conditions for liquefaction assessment." *Can. Geotech. J.* 57 (2): 263–276. https://doi.org/10.1139/cgj-2018-0287.

Beyzaei, C. Z., J. D. Bray, M. Cubrinovski, M. Riemer, and M. Stringer. 2018. "Laboratory-based characterization of shallow silty soils in southwest Christchurch." *Soil Dyn. Earthquake Eng.* 110 (Jul): 93–109. https://doi.org/10.1016/j.soildyn.2018.01.046.

Bong, T., and A. W. Stuedlein. 2018. "Effect of cone penetration conditioning on random field model parameters and impact of spatial variability on liquefaction-induced differential settlements." *J. Geotech. Geoenviron. Eng.* 144 (5): 04018018. https://doi.org/10.1061/(ASCE)GT.1943-5606.0001863.

Boone, S. J. 2010. "A critical reappraisal of 'preconsolidation pressure' interpretations using the oedometer test." *Can. Geotech. J.* 47 (3): 281–296. https://doi.org/10.1139/T09-093.

Boulanger, R. W. 1990. "Liquefaction behavior of saturated cohesionless soils subjected to unidirectional and bi-directional static and cyclic loads." Ph.D. thesis, Dept. of Civil & Environmental Engineering, Univ. of California.

Bray, J. D., and R. B. Sancio. 2006. "Assessment of the liquefaction susceptibility of fine-grained soils." *J. Geotech. Geoenviron. Eng.* 132 (9): 1165–1177. https://doi.org/10.1061/(ASCE)1090-0241(2006)132:9(1165).

Cappa, R., S. J. Brandenberg, and A. Lemnitzer. 2017. "Strains and pore pressures generated during cyclic loading of embankments on organic soil." *J. Geotech. Geoenviron. Eng.* 143 (9): 04017069. https://doi.org/10.1061/(ASCE)GT.1943-5606.0001721.

Cappellaro, C., M. Cubrinovski, J. D. Bray, G. Chiaro, M. F. Riemer, and M. E. Stringer. 2021. "Liquefaction resistance of Christchurch sandy soils from direct simple shear tests." *Soil Dyn. Earthquake Eng.* 141 (Feb): 106489. https://doi.org/10.1016/j.soildyn.2020.106489.

Chandrupatla, T. R., A. D. Belegundu, T. Ramesh, and C. Ray. 2002. Vol. 10 of *Introduction to finite elements in engineering*. Upper Saddle River, NJ: Prentice Hall.

Chang, W. J. 2011. "Evaluation of undrained shear strains in multidirectional horizontal shaking." *Soil Dyn. Earthquake Eng.* 31 (7): 906–920. https://doi.org/10.1016/j.soildyn.2011.02.002.

Chang, W. J., E. M. Rathje, K. H. Stokoe II, K. Hazirbaba. 2007. "In situ pore pressure generation behavior of liquefiable sand." *J. Geotech. Geoenviron. Eng.* 133 (8): 921–931. https://doi.org/10.1061/(ASCE)1090-0241(2007)133:8(921).

Cox, B., K. Stokoe, and E. Rathje. 2009. "An in -situ test method for evaluating the coupled pore pressure generation and nonlinear shear modulus behavior of liquefiable soils." *Geotech. Test. J.* 32 (1): 11–21. https://doi.org/10.1520/GTJ101484.

Cox, B. R. 2006. "Development of a direct test method for dynamically assessing the liquefaction resistance of soils in situ." Ph.D. thesis, Dept. of Civil, Architectural and Environmental Engineering, Univ. of Texas at Austin.

Cox, B. R., K. A. McLaughlin, S. van Ballegooy, M. Cubrinovski, R. Boulanger, and L. Wotherspoon. 2017. "In-situ investigation of false-positive liquefaction sites in Christchurch, New Zealand: St. Teresa's school case history." In *Proc., 3rd Int. Conf. Performance Based Design in Earthquake Geotechnical Engineering*. London: International Society for Soil Mechanics and Geotechnical Engineering.

Cubrinovski, M., D. Henderson, and B. A. Bradley. 2012. "Liquefaction Impacts in Residential Areas in the 2010-2011 Christchurch Earthquakes." In *Proc., One Year after 2011 Great East Japan Earthquake—Int. Symp. on Engineering Lessons Learned from the Giant Earthquake*, 811–824. Tokyo: Japan Association for Earthquake Engineering.

Cubrinovski, M., A. Rhodes, N. Ntritsos, and S. Van Ballegooy. 2019. "System response of liquefiable deposits." *Soil Dyn. Earthquake Eng.* 124 (Sep): 212–229. https://doi.org/10.1016/j.soildyn.2018.05.013.

Dadashiserej, A., A. Jana, A. W. Stuedlein, and T. M. Evans. 2022a. "Effect of strain history on the monotonic and cyclic response of natural and reconstituted silts." *Soil Dyn. Earthquake Eng.* 160 (Sep): 107329. https://doi.org/10.1016/j.soildyn.2022.107329.

Dadashiserej, A., A. Jana, A. W. Stuedlein, T. M. Evans, B. Zhang, Z. Xu, K. H. Stokoe II, and B. R. Cox. 2022b. "In-situ and laboratory cyclic response of an alluvial plastic silt deposit." In *Proc., 20th Int. Conf. on Soil Mechanics and Geotechnical Engineering*. Perth, WA, Australia: Australian Geomechanics Society.

Dahl, K. R., J. T. DeJong, R. W. Boulanger, R. Pyke, and D. Wahl. 2014. "Characterization of an alluvial silt and clay deposit for monotonic, cyclic, and post-cyclic behavior." *Can. Geotech. J.* 51 (4): 432–440. https://doi.org/10.1139/cgj-2013-0057.

Darendeli, M. B. 2001. "Development of a new family of normalized modulus reduction and material damping curves." Ph.D. dissertation, Dept. of Civil, Architectural and Environmental Engineering, Univ. of Texas at Austin.

DeJong, J. T., C. P. Krage, B. M. Albin, and D. J. DeGroot. 2018. "Work-based framework for sample quality evaluation of low plasticity soils." *J. Geotech. Geoenviron. Eng.* 144 (10): 04018074. https://doi.org/10.1061/(ASCE)GT.1943-5606.0001941.

Dobry, R., and T. Abdoun. 2015. "Cyclic shear strain needed for liquefaction triggering and assessment of overburden pressure factor Kσ." *J. Geotech. Geoenviron. Eng.* 141 (11): 04015047. https://doi.org/10.1061/(ASCE)GT.1943-5606.0001342.

Dobry, R., R. S. Ladd, F. Y. Yokel, R. M. Chung, and D. Powell. 1982. Vol. 138 of *Prediction of pore water pressure buildup and liquefaction of sands during earthquakes by the cyclic strain method*. Gaithersburg, MD: National Bureau of Standards.

Dobry, R., S. Thevanayagam, W. El-Sekelly, T. Abdoun, and Q. Huang. 2019. "Large-scale modeling of preshaking effect on liquefaction resistance, shear wave velocity, and CPT tip resistance of clean sand." *J. Geotech. Geoenviron. Eng.* 145 (10): 04019065. https://doi.org/10.1061/(ASCE)GT.1943-5606.0002080.

El-Sekelly, W., R. Dobry, T. Abdoun, and J. H. Steidl. 2017. "Two case histories demonstrating the effect of past earthquakes on liquefaction resistance of silty sand." *J. Geotech. Geoenviron. Eng.* 143 (6): 04017009. https://doi.org/10.1061/(ASCE)GT.1943-5606.0001654.

Fiegel, G. L., and B. L. Kutter. 1994. "Liquefaction mechanism for layered soils." *J. Geotech. Eng.* 120 (4): 737–755. https://doi.org/10.1061/(ASCE)0733-9410(1994)120:4(737).

Finn, W. D., P. L. Barnaby, and D. J. Pickering. 1970. "Effect of strain history on liquefaction of sand." *J. Soil Mech. Found. Div.* 96 (6): 1917–1934. https://doi.org/10.1061/JSFEAQ.0001478.

Gohl, W. B., J. A. Howie, and C. E. Rea. 2001. "Use of controlled detonation of explosives for liquefaction testing." In *Proc., 4th Int. Conf. on Recent Advances in Geotechnical Earthquake Engineering and Soil Dynamics*. Rolla, MO: Univ. of Missouri-Rolla.

Heelan, P. A. 1953. "Radiation from a cylindrical source of finite length." *Geophysics* 18 (3): 685. https://doi.org/10.1190/1.1437923.

Hsu, C. C., and M. Vucetic. 2006. "Threshold shear strain for cyclic pore-water pressure in cohesive soils." *J. Geotech. Geoenviron. Eng.* 132 (10): 1325–1335. https://doi.org/10.1061/(ASCE)1090-0241(2006)132:10(1325).

Idriss, I. M., and R. W. Boulanger. 2008. "Soil liquefaction during earthquakes." In *Monograph MNO-12*. Oakland, CA: Earthquake Engineering Research Institute.

Isenhower, W. M., and K. H. Stokoe II. 1981. "Strain-rate dependent shear modulus of San Francisco Bay mud." In Vol. 2 of *Proc., Int. Conf. Recent Advances Earthquake Engineering Soil Dynamics*, 597–602. Rolla, MO: Univ. of Missouri-Rolla.

Ishihara, K. 1968. "Propagation of compressional waves in a saturated soil." In *Proc., Int. Symp. Wave Propagation and Dynamic Properties Earth Material*, 195–206. Albuquerque, NM: University of New Mexico Press.

Jana, A. 2021. "Use of controlled blasting to quantify the dynamic, in-situ, nonlinear inelastic response of soils." Ph.D. thesis, School of Civil and Construction Engineering, Oregon State Univ.

Jana, A., A. M. Donaldson, A. W. Stuedlein, and T. M. Evans. 2021. "Deep, in-situ nonlinear dynamic testing of soil with controlled blasting: Instrumentation, calibration, and example application to a plastic silt deposit." *Geotech. Test. J.* 44 (5): 20190426. https://doi.org/10.1520/GTJ20190426.

Jana, A., and A. W. Stuedlein. 2021a. "Dynamic, in-situ, nonlinear-inelastic response and post-cyclic strength of a plastic silt deposit." *Can. Geotech. J.* 59 (1): 111–128. https://doi.org/10.1139/cgj-2020-0652.

Jana, A., and A. W. Stuedlein. 2021b. "Dynamic in-situ response of a deep, medium dense sand deposit." *J. Geotech. Geoenviron. Eng.* 147 (6): 04021039. https://doi.org/10.1061/(ASCE)GT.1943-5606.0002523.

Jana, A., and A. W. Stuedlein. 2021c. "Monotonic, cyclic and post-cyclic response of an alluvial plastic silt deposit." *J. Geotech. Geoenviron. Eng.* 147 (3): 04020174. https://doi.org/10.1061/(ASCE)GT.1943-5606.0002462.

Kammerer, A. M., J. M. Pestana, and R. B. Seed. 2002. *Undrained response of Monterey 0/30 sand under multidirectional cyclic simple shear loading conditions*. Geotechnical Engineering Rep. No. UCB/GT/02-01. Berkeley: Univ. of California.

Kim, C. 2012. "Development of the spectral-analysis-of-body-waves (SABW) method for downhole seismic testing with boreholes or penetrometers." Ph.D. dissertation, Dept. of Civil, Architectural and Environmental Engineering, Univ. of Texas at Austin.

Kishida, T., D. Park, R. L. Sousa, R. Armstrong, and Y. J. Byon. 2020. "Modulus reductions of dam embankment materials based on downhole array time series." *Earthquake spectra* 36 (1): 400–421. https://doi.org/10.1177/8755293019878182.

Kishida, T., and C. C. Tsai. 2021. "Wave velocities depending on shear strain, directionality, and excess pore water pressure from wildlife liquefaction array." *Bull. Earthquake Eng.* 19 (6): 2371–2388. https://doi.org/10.1007/s10518-021-01074-4.

Koester, J. P. 1994. "The influence of fines type and content on cyclic strength." In *Ground failures under seismic conditions*, 17–33. Reston, VA: ASCE.

Kurtulus, A., and K. H. Stokoe. 2008. "In situ measurement of nonlinear shear modulus of silty soil." *J. Geotech. Geoenviron. Eng.* 134 (10): 1531–1540. https://doi.org/10.1061/(ASCE)1090-0241(2008)134:10(1531).

Ladd, R. S. 1977. "Specimen preparation and cyclic stability of sands." *J. Geotech. Eng. Div.* 103 (6): 535–547. https://doi.org/10.1061/AJGEB6.0000435.

Lee, K. L., and H. B. Seed. 1967. "Cyclic stress conditions causing liquefaction of sand." *J. Soil Mech. Found. Div.* 93 (1): 47–70. https://doi.org/10.1061/JSFEAQ.0000945.

Matsuda, H., T. T. Nhan, and R. Ishikura. 2013. "Prediction of excess pore water pressure and post-cyclic settlement on soft clay induced

by uni-directional and multi-directional cyclic shears as a function of strain path parameters." *Soil Dyn. Earthquake Eng.* 49 (Jun): 75–88. https://doi.org/10.1016/j.soildyn.2013.01.010.

Mayne, P. W., 2007. *Cone penetration testing: A synthesis of highway practice*. NCHRP Rep. No. 368. Washington, DC: Transportation Research Board.

Mortezaie, A., and M. Vucetic. 2016. "Threshold shear strains for cyclic degradation and cyclic pore water pressure generation in two clays." *J. Geotech. Geoenviron. Eng.* 142 (5): 04016007. https://doi.org/10.1061/(ASCE)GT.1943-5606.0001461.

Mulilis, J. P., H. B. Seed, C. K. Chan, J. K. Mitchell, and K. Arulanandan. 1977. "Effects of sample preparation on sand liquefaction." *J. Geotech. Eng. Div.* 103 (2): 91–108. https://doi.org/10.1061/AJGEB6.0000387.

Oda, M., K. Kawamoto, K. Suzuki, H. Fujimori, and M. Sato. 2001. "Microstructural interpretation on reliquefaction of saturated granular soils under cyclic loading." *J. Geotech. Geoenviron. Eng.* 127 (5): 416–423. https://doi.org/10.1061/(ASCE)1090-0241(2001)127:5(416).

Olson, S. M., S. F. Obermeier, and T. D. Stark. 2001. "Interpretation of penetration resistance for back-analysis at sites of previous liquefaction." *Seismol. Res. Lett.* 72 (1): 46–59. https://doi.org/10.1785/gssrl.72.1.46.

Park, T., and M. L. Silver. 1975. *Dynamic soil properties required to predict the dynamic behavior of elevated transportation structures*. Washington, DC: US Department of Transportation.

Polito, C. P., and J. R. Martin II. 2001. "Effects of nonplastic fines on the liquefaction resistance of sands." *J. Geotech. Geoenviron. Eng.* 127 (5): 408–415. https://doi.org/10.1061/(ASCE)1090-0241(2001)127:5(408).

Rathje, E., R. Phillips, W. J. Chang, and K. H. Stokoe. 2001. "Evaluating nonlinear response in situ." In *Proc., 4th Int. Conf. on Recent Advances in Geotechnical Earthquake Engineering and Soil Dynamics*. Rolla, MO: Missouri Univ. of Science and Technology.

Roberts, J. N., K. H. Stokoe, S. Hwang, B. R. Cox, Y. Wang, F. M. Menq, and S. van Ballegooy. 2016. "Field measurements of the variability in shear strain and pore pressure generation in Christchurch soils." In *Proc., 5th Int. Conf. on Geotechnical and Geophysical Site Characterization*. Sydney, NSW, Australia: Australian Geomechanics Society.

Robertson, P. 2009. "Interpretation of cone penetration tests—A unified approach." *Can. Geotech. J.* 46 (11): 1337–1355. https://doi.org/10.1139/T09-065.

Sahadewa, A., D. Zekkos, R. D. Woods, and K. H. Stokoe. 2015. "Field testing method for evaluating the small-strain shear modulus and shear modulus nonlinearity of solid waste." *Geotech. Test. J.* 38 (4): 20140016–20140441. https://doi.org/10.1520/GTJ20140016.

Sanin, M. V., and D. Wijewickreme. 2006. "Cyclic shear response of channel-fill Fraser River Delta silt." *Soil Dyn. Earthquake Eng.* 26 (9): 854–869. https://doi.org/10.1016/j.soildyn.2005.12.006.

Seed, H. B., and I. M. Idriss. 1971. "Simplified procedure for evaluating soil liquefaction potential." *J. Geotech. Eng.* 97 (9): 1249–1273. https://doi.org/10.1061/JSFEAQ.0001662.

Seed, H. B., G. R. Martin, and R. M. Pyke. 1978. "Effect of multidirectional shaking on pore pressure development in sands." *J. Geotech. Eng. Div.* 104 (1): 27–44. https://doi.org/10.1061/AJGEB6.0000575.

Stokoe K. H., and J. C. Santamarina. 2000. "Seismic-wave-based testing in geotechnical engineering." In *Proc., GeoEngineering 2000*, 1490–1536. Melbourne, Australia: Technomic.

Stokoe, K. H., II, B. R. Cox, P. Clayton, and F. M. Menq. 2017. "NHERI@UTEXAS experimental facility: Large-scale mobile shakers for natural-hazards field studies." In *Proc., 16th World Conf. on Earthquake Engineering*. San Jose, CA: Curran Associates.

Stokoe, K. H., II, S. K. Hwang, J. K. Lee, and R. D. Andrus. 1995. "Effects of various parameters on the stiffness and damping of soils at small to medium strains." In Vol. 2 of *Proc., Int. Symp., Pre-Failure Deformation of Geomaterials*. Hokkaido, Japan: Sapporo.

Stuedlein, A., M. Evans, A. Dadashiserej, and A. Jana. 2021. "Oregon state university blast array with T-Rex." In *Collaborative research: Bridging the in-situ and elemental cyclic response of transitional soils*. https://doi.org/10.17603/ds2-c74j-e947.

Stuedlein, A. W., A. Dadashiserej, A. Jana, and T. M. Evans. 2023. "Liquefaction susceptibility and cyclic response of intact nonplastic and plastic silts." *J. Geotech. Geoenviron. Eng.* 149 (1): 04022125. https://doi.org/10.1061/(ASCE)GT.1943-5606.0002935.

Vaid, Y. P. 1994. "Liquefaction of silty soils." In *Ground failures under seismic conditions, GSP No. 44*, 1–16. New York: ASCE.

Vardanega, P. J., and M. D. Bolton. 2013. "Stiffness of clays and silts: Normalizing shear modulus and shear strain." *J. Geotech. Geoenviron. Eng.* 139 (9): 1575–1589. https://doi.org/10.1061/(ASCE)GT.1943-5606.0000887.

Vucetic, M., and R. Dobry. 1991. "Effect of soil plasticity on cyclic response." *J. Geotech. Eng.* 117 (1): 89–107. https://doi.org/10.1061/(ASCE)0733-9410(1991)117:1(89).

Vucetic, M., and K. Tabata. 2003. "Influence of soil type on the effect of strain rate on small-strain cyclic shear modulus." *Soils Found.* 43 (5): 161–173. https://doi.org/10.3208/sandf.43.5_161.

Wang, B., C. Yao, Z. Liu, H. Fan, and H. Xiao. 2019. "Development of an energy-based EPWP generation model under different drainage conditions." *Earth Environ. Sci.* 304 (2): 022053. https://doi.org/10.1088/1755-1315/304/2/022053.

Wang, Y., and K. H. Stokoe. 2022. "Development of constitutive models for linear and nonlinear shear modulus and material damping ratio of uncemented soils." *J. Geotech. Geoenviron. Eng.* 148 (3): 04021192. https://doi.org/10.1061/(ASCE)GT.1943-5606.0002736.

Wijewickreme, D., A. Soysa, and P. Verma. 2019. "Response of natural fine-grained soils for seismic design practice: A collection of research findings from British Columbia, Canada." *Soil Dyn. Earthquake Eng.* 124 (Sep): 280–296. https://doi.org/10.1016/j.soildyn.2018.04.053.

Yniesta, S., and M. Janati-Idrissi. 2021. "Integration of viscoplastic effects in a one-dimensional constitutive model for ground response analysis." *Can. Geotech. J.* 58 (4): 468–478. https://doi.org/10.1139/cgj-2019-0717.

Yost, K. M., B. R. Cox, L. Wotherspoon, R. W. Boulanger, S. van Ballegooy, and M. Cubrinovski. 2019. "In situ investigation of false-positive liquefaction sites in Christchurch, New Zealand: Palinurus road case history." In *Geo-congress 2019: Earthquake engineering and soil dynamics*, 436–451. Reston, VA: ASCE.

Zeghal, M., and A. W. Elgamal. 1994. "Analysis of site liquefaction using earthquake records." *J. Geotech. Eng.* 120 (6): 996–1017. https://doi.org/10.1061/(ASCE)0733-9410(1994)120:6(996).

Zhang, B. 2020. "Improvements to field liquefaction testing with large mobile shakers." Ph.D. thesis, Dept. of Civil, Architectural, and Environmental Engineering, Univ. of Texas.

Zhang, B., et al. 2021. "Collaborative study on dynamic response of transitional soils." In *Collaborative research: Bridging the in-situ and elemental cyclic response of transitional soils*. https://doi.org/10.17603/ds2-81g3-ef87.